A mm-Scale Aeroelastic Oscillation-Based Anemometer

Ian McKay

Submitted to the Department of Mechanical Engineering
In Partial Fulfillment of the Requirements for the
Degree of

Bachelor of Science
at the
Massachusetts Institute of Technology

June 2012

Signature of Author.....
Department of Mechanical Engineering
February 7, 2012

Certified by.....
Gareth McKinley
Associate Department Head
Professor of Teaching Innovation in Mechanical Engineering
Thesis Supervisor

Accepted by.....
John H. Lienhard V
Collins Professor of Mechanical Engineering
Chairman, Undergraduate Thesis Committee

A mm-Scale Aeroelastic Oscillation-Based Anemometer

Ian McKay

Submitted to the Department of Mechanical Engineering
In Partial Fulfillment of the Requirements for the
Degree of

Bachelor of Science
at the
Massachusetts Institute of Technology

February 2012

Abstract

The flutter of a thin filament can provide a good indication of fluid velocity at small scales. By combining a 'fishtail'-shaped filament's aeroelastic and vortex-forced flutter modes, its oscillation frequency can be confined to scale smoothly with fluid velocity. This principle has been used to produce a low-cost, mm-scale anemometer that measures air flow to ±(5% + 0.5m/s) from 1-25m/s. This paper describes the prototype and the experiments that informed its design, and shows how a similar system could operate at far smaller scales than existing anemometers.

Nomenclature

A*: Aspect ratio L/H_{max} (dimensionless)
A: Tube or nozzle cross-sectional area (m^2)
a: Acceleration (m/s^2)
C_L: Coefficient of Lift (dimensionless)
C_D: Coefficient of Lift (dimensionless)
D: Unit-span flexural rigidity, $Eh^3 / (12(1-v^2))$ (N*m)
d: Bluff body or nozzle diameter (m)
E: Young's Modulus (N/m^2)
e: Vortex Energy Density (J/m^3)
Eta: Nozzle pressure recovery factor (dimensionless)
F: Tensile force (N)
f: Oscillation frequency (Hz)
H: Filament height (m)
h: Filament thickness (m)
J: Linear nozzle slope (dimensionless)
L: Filament length (m)
M*: Mass ratio p_f*L/m (dimensionless)
Ma: Mach Number U/U_{sound} (dimensionless)
mu: Dynamic Viscosity (kg/m*s)
m: Filament plane density (kg/m^2)
P: Pressure (Pa)
p_f: Fluid Density (kg/m^3)
p_s: Filament Density (kg/m^3)
Re: Reynold's number pUd/mu (dimensionless)
r: Second moment of area, (dimensionless)
S: Filament area (m^2)
St: Strouhal number fd/U (dimensionless)
T: Tensile strength (Pa)
theta: Angular deflection (rad)
U*: Reduced velocity, $L*U*(m/D)^{1/2}$ (dimensionless)
U: Fluid velocity (m/s)
U_C: Upper critical velocity (m/s)
U_D: Lower critical velocity (m/s)
v: Poisson Ratio (dimensionless)
x: length coordinate along filament (m)
y(x): Transverse deflection (m)

ADC: Analog-to-Digital Converter
CAD: Computer-Aided Design
DAC: Digital-to-analog-Converter
DFT: Discrete Fourier Transform
FFT: Fast Fourier Transform
IC: Integrated Circuit
LCD: Liquid Crystal Display
LED: Light-Emitting Diode
PC: Personal Computer
PCB: Printed Circuit Board
UAV: Unmanned Aerial Vehicle
uC: Microcontroller
USB: Universal Serial Bus

Thesis Supervisor: Gareth H. McKinley
Title: Professor of Teaching Innovation in Mechanical Engineering

Contents

1. Introduction and Background 4
2. Studies 6
2.1 Free Stream Frequency-Velocity Relation 6
2.2 Filament Shape 6
2.3 Vortex Forcing 10
2.4 Filament Material 12
2.5 Nozzle Integration 14
2.6 Scaling Limits 16
2.7 Second Onset Velocity 17
3. Prototype Design 18
3.1 Experimental Optimization 19
3.2 Flutter Detection 20
3.3 A Working Prototype 21
4. Discussion 25
4.1 Performance Comparison with Available Anemometers 25
4.2 Future Improvements 27
4.3 Likely Applications 27
4.4 Implications for Aeroelastic Energy Harvesters 28
4.5 Theoretical Contributions to 'The Flag Problem' 28
5. Conclusions 29
6. Appendices 30
6.1 Proof-of-Concept 'Fish Anemometer' 30
References 36

Tables

1 Summary of Measured and Literature Properties of Different Plastic Films 13
2 Working Prototype Cost Breakdown 24
3 Cost Breakdown of Hypothetical Mark-II Prototype 26
4 Performance Comparison with Available Anemometers 27

Figures

1 Basic Parallel Flow Flag Configuration 4
2 Free Stream Flutter Behavior 6
3 A 'Fishtail' Shaped Flag 7
4 Transition U* Versus Fluid Velocity 8
5 Deflection with Uniform Pressure Loading 9
6 Flag with a Saturating Exponential Shape 10
7 Onset Velocity as an Activation Energy 10
8 Filament Placement in the Vortex Street 11
9 Vortex-Forced Flutter Behavior 12
10 Dimensional Vortex-Forced Flutter Behavior 12
11 Filament Material and Onset Velocity 13
12 Schematic of a Nozzle-Integrated System 14
13 Several Linear Test Nozzles 15
14 Dimensionless Nozzle Performance Comparison 15
15 Micro-Anemometer Scaling Considerations 15
16 A mm-Scale Filament 17
17 A mm-Scale Filament 17
18 Second Onset Velocity U* 17
19 Fishtail Filament Failure Point 18
20 Filament Thickness Considerations 19
21 Nozzle- and Bluff Body- Integration 19
22 Nozzle- and Bluff Body-Optimization 20
23 Prototype Sensor Systems 20
24 The Working Prototype 21
25 The Working Prototype CAD 21
26 The Working Prototype CAD 22
27 Basic Electrical System Schematic 22
28 Anemometer Control Code Flowchart 23
29 Performance of the Integrated Prototype 24
30 A Hypothetical Mark-II Prototype 25
31 Transverse Flow Orientation 26
32 Proof-of-Concept Prototype 30
33 Proof-of-Concept Hard-Coded Correlation 30
34 Proof-of-Concept Prototype Internals 31
35 Proof-of-Concept Basic Flowchart 31
36 Proof-of-Concept Electrical Schematic 32
37 Proof-of-Concept Software Flowchart 33
38 Proof-of-Concept Sensor Electronics 34
39 Proof-of-Concept Video Stills 34

1. Introduction and Background

A streamer suspended in a moving fluid flutters at a frequency that increases with the velocity of the fluid. Most people are familiar with this phenomenon from watching flags; on calm days, flags wave slowly back and forth, while on windy days they flap much more quickly. This type of aeroelastic flutter is a well-studied problem in the interaction of structures and fluids. Various efforts have clarified most aspects of flutter behavior, including the origin of the flutter instability and the tendency of the oscillation frequency to increase with fluid velocity [*Bao et al. 2010, Michelin et al. 2008*]. But while fluttering flags are commonly used as an informal indicator of wind speed, the possibility of an anemometer based on aeroelastic flutter hasn't been fully evaluated. This is surprising; fluttering filaments ('flags') have no mechanical joints, are simple to manufacture, and have good scaling potential. These factors make aeroelastic flutter a promising basis for a new class of low-cost, miniature flowmeters.

Typical anemometers rely on lift or drag forces to indicate wind speed. For rotary vane or ball-and-cup anemometers, the lift and drag coefficients C_L and C_D, respectively, each scale with the characteristic length L of the rotor or blade, $C_{D,L} \sim 1/L^2$. By contrast, the scaling factors that define the flutter of a flag involve only dimensional ratios, not the absolute size of the flag. As determined by [*Mahadevan and Argentina 2004*], the critical wind velocity U_C for the flutter of a flag scales with the flag thickness h and length L as $U_C \sim (h/L)^{1.5}$. Because of the favorable scaling, an anemometer based on flutter phenomena could theoretically work at far smaller scales than traditional systems based on lift- or drag-forces.

In this work the aeroelastic oscillation-based flowmeter consists of a small filament suspended parallel to fluid flow. As the filament flutters, its fundamental frequency is measured and compared to a frequency-fluid velocity correlation developed for the filament. The result is a small, low cost anemometer with reasonable accuracy; an 8mm prototype system based on this approach reliably measures air flow to ±(5%+0.5m/s) from 1-25m/s, and costs less than $5. The small size and low cost could make this system useful in various applications unsuitable for traditional anemometers.

Though simple in principle, an aeroelastic oscillation-based flowmeter requires a filament system with both low flutter onset velocity and a monotonic flutter frequency – air velocity correlation. Practically, these challenges require a design that is both inherently unstable and inclined to oscillate with one dominant mode over a range of fluid velocities. This paper discusses the theoretical and experimental considerations in the system design, the details of two working prototypes, and the prospects for further developments in aeroelasticity-based flow measurement.

Why Flags Flap

The wealth of literature on the 'flag problem', as it is known, is a good starting point for designing a flowmeter based on aeroelastic flutter. The problem has been addressed in contexts as varied as fish locomotion, energy harvesting, vehicle aerodynamics, and the mechanics of snoring [*Shen et al. 2003, Huang 1995, Kornecki 1976, Taylor et al. 2001*]. While different models have been proposed, the flag's equation of motion is generally formulated as a balance between the stabilizing bending stiffness of the flag and a destabilizing transverse fluid loading, in addition to the flag's inertia and tensional fluid loading. The consensus conclusion is that the flutter of a flag results from a resonant bending instability above a critical wind speed U_C, which can be estimated by solving a homogenous eigenvalue problem [*Manela et al. 2009, Mahadevan and Argentina 2004*].

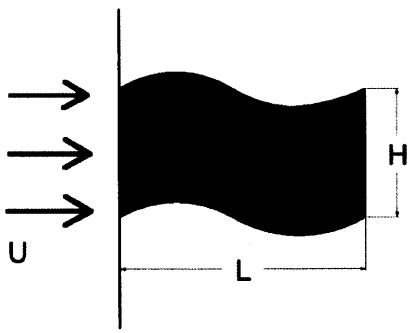

Figure 1: *A rectangular flag of length L and height H immersed in a fluid of velocity U. This the commonly-analyzed 'flag problem' and is also the configuration of the experiments presented in section 2.1.*

Mahadevan and Argentina's linearized treatment of a flag as a 2-d airfoil is a good example of both the utility and limitations in applying the theory behind 'the flag problem' to a real system. Their model reflects the dependencies governing U_C and the observed variation in the flutter mode with the mass ratio p_f*L/m, where L is the flag length, m its mass per unit surface, and p_f the fluid density. In particular, they accurately predict that U_C decreases with increasing aspect ratio A* = length L/height H and decreasing plate thickness h and Young's Modulus E. However, their model consistently underestimates the U_C of real flags, and fails to predict the subcritical bifurcation that can lead to hysteresis in the transition to flutter. While others have examined the 3-d problem and achieved better agreement with experiments [*Eloy et al. 2008*],

and numerical solutions of Navier-Stokes can simulate the flapping instability for rectangular flags [*Zhu et al. 2002*], the state of the art is better suited to qualitative than quantitative predictions of flag behavior.

Despite these limitations, previous work on the 'flag problem' informs the basic design of an aeroelasticity-based anemometer in several ways. In order to maximize its functional range, the anemometer filament's U_C must be as low as possible. The hysteresis in the transition to flutter, which could confuse automatic measurement, must also be minimized. As suggested in multiple works, both of these can be accomplished by increasing the filament's aspect ratio A*. U_C can also be reduced by decreasing the flag's bending moment $D = Eh^3 / 12(1-v^2)$, where v is the Poisson ratio of the flag material [*Eloy et al. 2008, Bao et al.* 2010]. Practically, this is done by using a thinner or 'softer' (lower E) material.

Theory also suggests how to reduce the impact of transitions between dominant flutter modes, which can lead to a non-monotonic relationship between fluid velocity and the measured flutter frequency *[Bao et al. 2010, Zhang et al. 2009]*. Filaments of smaller A* experience mode transitions at a higher velocity, leading to fewer 'jumps' in a given measurement range [*Mahadevan and Argentina 2004]*. More practically, work by [*Eloy et al. 2008*] suggests how to achieve a lower mode without sacrificing a favorable U_C. Decreasing the mass ratio $M^* = p_f * L/m$, where p_f is the fluid density and m is the filament mass per area, has been shown to keep the primary oscillation at a lower mode.

The Influence of Upstream Instability

Another complication in applying the theory from 'the flag problem' to a real device is the influence of upstream instability. As pointed out by [*Manela et al. 2009*], the vortex street shed by a flagpole adds a forcing term to a flag's equation of motion. Because an oscillation-based anemometer requires a protective housing as well as a 'flagpole' for support, it's inevitable that the flutter of the anemometer filament will be affected by turbulence from neighboring objects. However, as shown by [*Wang et al. 2009*], this forcing term can serve to make the flapping more regular. Indeed, Wang shows that in one case, a 1-d filament in a vortex street oscillates at the von-Karman vortex shedding frequency, which increases predictably with velocity within certain Re ranges [*R.W. Miller, 2010*]. While a purely vortex-forced flag motion requires too large of a bluff body for a miniature flowmeter, the effect of a bluff body can still be used to 'smooth' an otherwise irregular air velocity– flutter frequency correlation.

2. Studies

A variety of experiments were performed to find the optimal flag size, shape and material for use in a small oscillation-based anemometer. Further experiments with different sized bluff-bodies (vortex-shedding structures) and nozzles also informed the design of the final integrated system. All flutter experiments reported here were performed in a 30cmx30cm wind tunnel, with the air velocity referenced against a pitot tube with a precision of ~±0.1m/s. While many observations presented in this section apply in general to the flutter problem, or to a future MEMs scale device, the majority directly informs the design of an anemometer system.

2.1 Free-Stream Frequency-Velocity Correlation

While the flutter of rectangular flags is a very common subject of fluid experiments, quantitative flutter frequency-velocity correlations are not typically made. Initial experiments on the flutter behavior of rectangular flags in free stream were necessary to clarify the challenges in building an oscillation-based anemometer. These show that the primary challenges to aeroelasticity based windspeed measurement are i) high critical velocity U_C, ii) hysteresis in the transition to flutter; U_C, the critical velocity as fluid velocity increases, is greater than U_D, the critical velocity as it decreases, and iii) a non monotonic relationship between flutter frequency and fluid velocity.

Experiments were conducted on rectangular nylon flags with h = 50um, H = 6mm, and D = $9*10^{-5}$ Nm. Flags were positioned on thin carbon strands, and their flutter frequency was measured discretely with a photointerrupt laser on the flag centerline, at a position x = ¾ L. Results are presented in terms of the non-dimensional reduced velocity $U^* = L*U*(m/D)^{1/2}$.

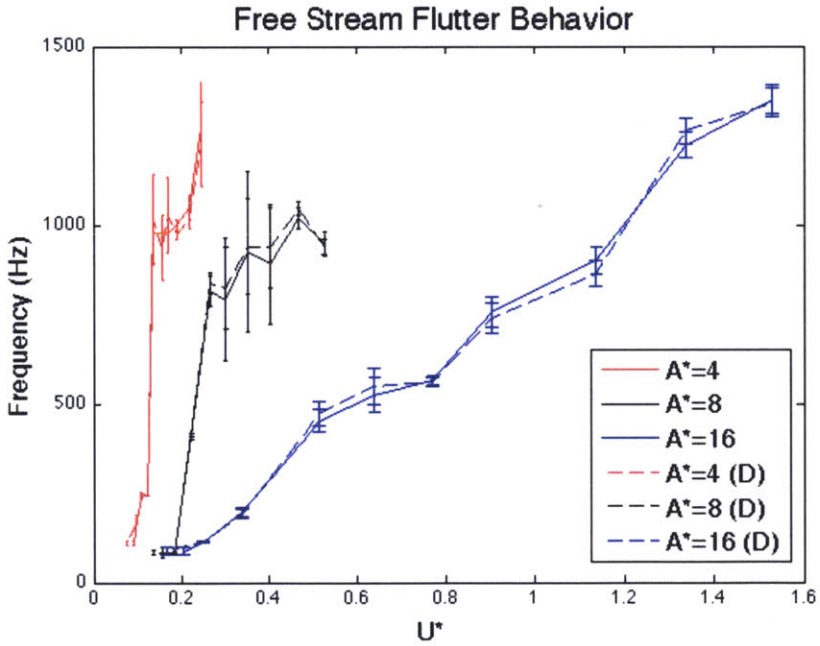

Figure 2: *Free stream flutter behavior of rectangular flags of different A*. Data for both upward (solid line) and downwards (dotted line) paths are shown. In dimensional terms these U_C were 6.2, 3.6, and 2.2 m/s for A* = 4, 8, and 16, respectively. This data is further discussed in section 2.7.*

2.2 The Effect of Filament Shape

Most prior investigations of flutter have focused on the behavior of elongated rectangular filaments. However, other geometries may be advantageous to an oscillation-based anemometer in terms of onset velocity and mode shape. Of particular interest is a 'fishtail' filament shape, wide at the back and tapering towards the flagpole. In one experiment, [*Beal et al., 2006*] found the fishtail shape to be naturally unstable, especially in a Von-Karman wake. Fascinatingly, [*Beal et al., 2006*] also found that an anesthetized fish was able to extract thrust from the vortex street and even move upstream. Because a naturally unstable shape facilitates flutter-based measurement at lower wind speeds, the biomimetic 'fishtail' filament shape was evaluated for incorporation in an oscillation-based anemometer.

Onset Velocity

[*Pang, 2010*] conducted experiments on elongated trapezoidal filaments, some of which generally match the 'fishtail' shape. [*Pang, 2010*] cut trapezoids from rectangular filaments of fixed A*, and described the trapezoid shapes via the non-dimensional second moment of area, defined as

$$r = \int_0^L \frac{H(x)x^2}{SL^2} dx$$

Where H(X) is the flag height as a function of distance from the flagpole, and S is the total filament area. It follows that r = 1/3 corresponds to a rectangular filament, while r > 1/3 is characteristic of a diverging (fishtail shape) filament, and r < 1/3 is characteristic of a converging (pointed) filament.

As might be expected, [*Pang, 2010*] found that the 2nd moment r influenced both onset velocity and the shape of oscillation. In particular, the onset velocity U_D, the fluid velocity at the transition from flutter, decreased monotonically with increasing r. The hysteresis width U_C - U_D decreased to a minimum at r = 1/3 and then increased again with increasing r.

While [*Pang, 2010*] made observations suggesting that a 'fishtail' (r>1/3) shape might be advantageous because of its greater instability (and hence lower U_D), those experiments don't offer great enough resolution to inform choice of r for an anemometer system. Moreover, though [*Pang, 2010*] notes that filaments of greater r tended to bend towards their thinner, front ends, no note was made on the influence on the mode or regularity of flapping frequency.

This motivated a series of experiments on 'fishtail' shaped flags. 17 filaments were cut out of nylon sheeting with E = 36 GPa, v = .35, and h = 50um, all with a length of 15mm. Filaments were tested in the 30cmx30cm wind tunnel as in the initial experiments. Unlike [*Pang, 2010*], the filaments were not all made with the same overall span area, so that the effects of both H_1 and H_2, the front and rear heights, could be independently related to the effect of A*.

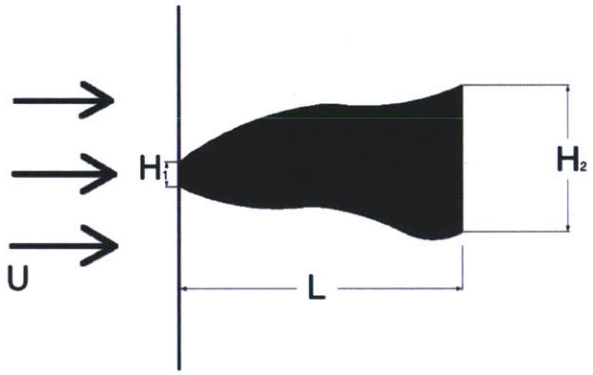

Figure 3: *The filament measurements used in the onset velocity experiments*

As shown in figure 4A, both onset velocities decrease with increasing r for r>1/3. In contrast with the [*Pang, 2010*] data, the hysteresis width in fact decreased with increasing r. This is perhaps more consistent with data from [*Bao et al.* 2010], who noted that the hysteresis width increased with smaller aspect ratio A*, which was proportional to the H_1 of their rectangular flags.

The comparison of length ratios H_1/L and H_2/L in figure 2B show that critical velocity scales almost exclusively with H_1/L (figure 4B). In fact, of the geometric parameters A*, r, H_1/L and H_2/L, H_1/L was seen to correlate most strongly with a low onset velocity.

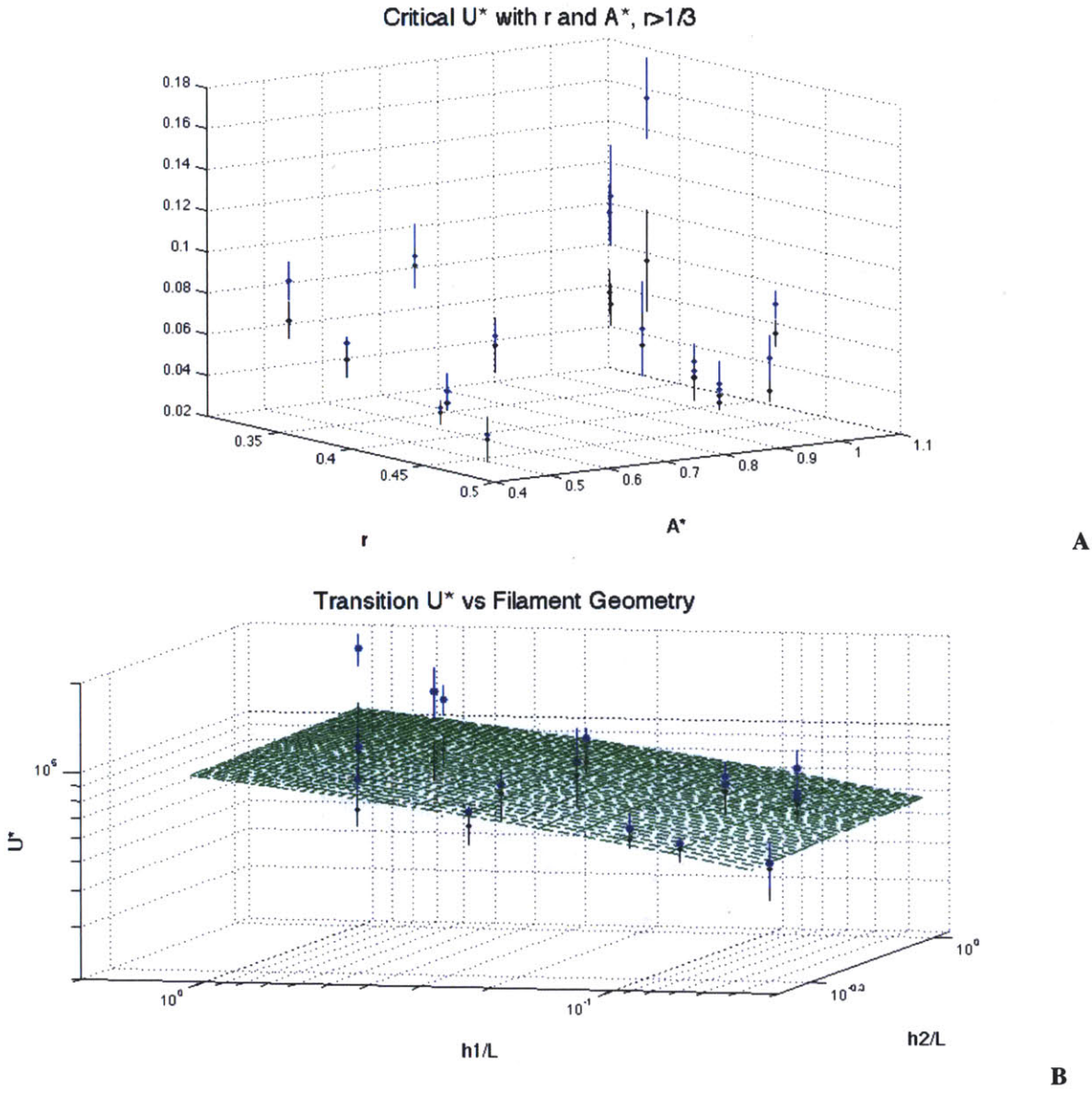

Figure 4: *The influence of filament geometry on reduced onset velocities U_C* (black) and U_D* (blue). In A, it's clear that the hysteresis U_C-U_D>0 depends more on A* than on r. In B, notice the log_{10} scale. The onset velocities all lie near the plane $U^*=1.1+.15*log(.6*H_1/L)+.05*log(H_2/L)$.*

Flexing Point

Another effect of a 'fishtail' filament shape is to bias the filament bending towards the front end. In the case of a trapezoidal 'fishtail' shaped flag under uniform pressure loading P, $H_1 \ll H_2$ and the deflection per length y(x) can be estimated via classical plate theory, $\nabla^2\nabla^2 y(x) = P/D$. The instantaneous small deflection is that of a variable-width cantilever plate.

$$y(x) = \frac{PH_2x^2}{120LDH(x)}(120L^3 - 10L^2x + x^3)$$

The deflection profiles predicted by this approach for different filament geometries are compared with the results of [*Pang, 2010*] in figure 5. As shown, the greatest flexure $\frac{d^2y}{dx^2}$ in the $H_2/H_1 = 5$ filament occurs at x = 0.1L, while the greatest flexure in the $H_2/H_1 = 0.5$ filament is at x = 0.45L.

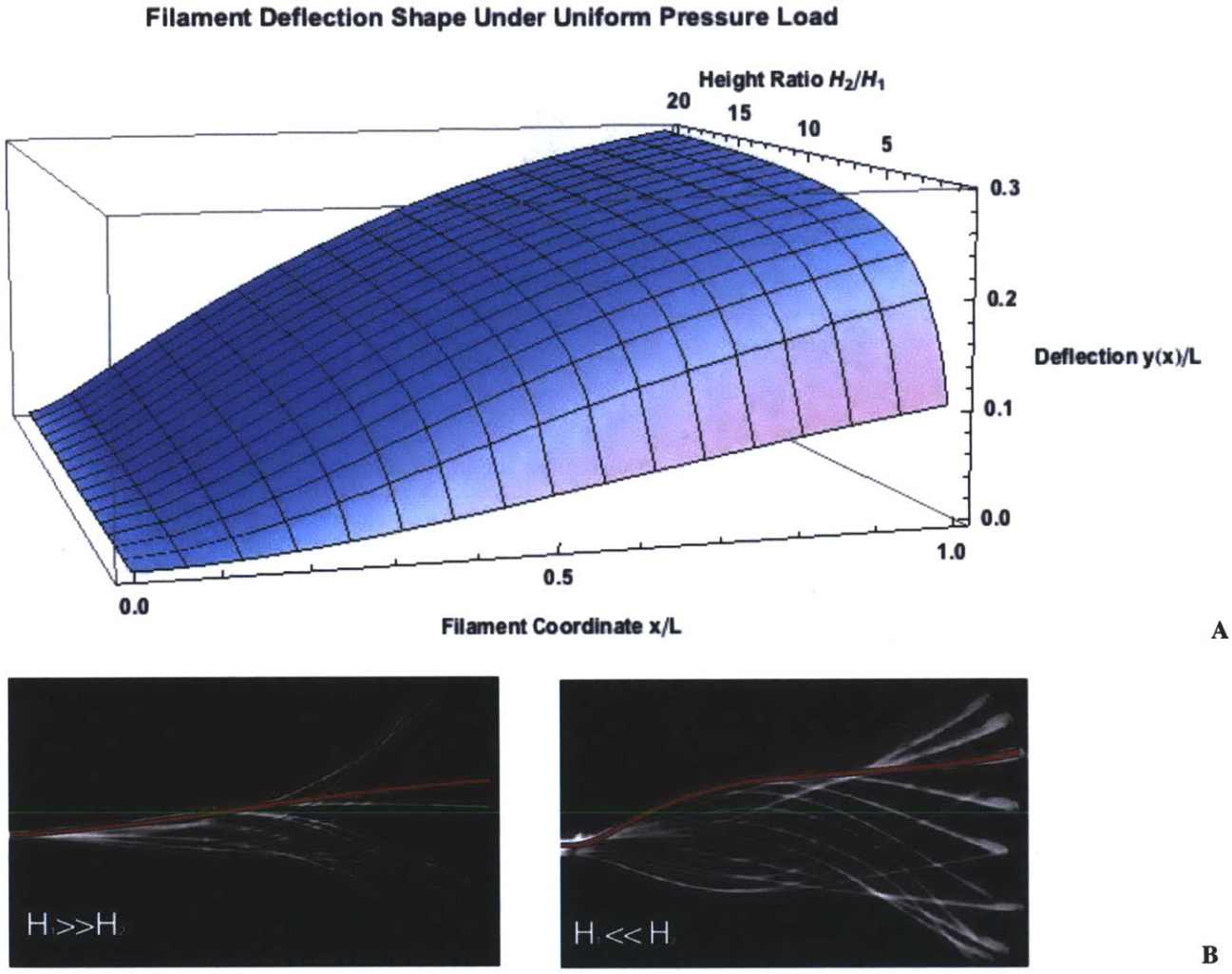

Figure 5: *A: A model for the deflection of a tapered plate of length L under uniform pressure loading in terms of various front to back height ratios H_2/H_1. B: Comparison with experimental results for the flutter mode shape of trapezoidal flags taken by [Pang, 2010]. The left photograph in B is the flutter of an elongated trapezoidal filament of $H_2/H_1 << 1$, the right is a filament with $H_2/H_1 >> 1$. Lines are drawn on the photographs to emphasize the median positions based on the deflection at x = L. Interestingly, it is at these median positions that the filament's curvature most closely matches the uniform pressure loading condition modeled in A.*

This bias towards front-end deflection could be beneficial to a fluid measurement system for two reasons. The first involves the detection strategy. Because the low cost photo-microsensors used to detect filament frequency (see section 3.2) have fixed beam widths many times greater than the filament thickness h, a wider bifurcation at lower x allows much more flexibility in sensor placement along the filament. In particular, the larger displacement at low x along the filament makes it easier to place the sensor at low x, assuring measurement of only the lowest flutter mode. Moreover, greater overall flutter amplitude seen with the r>>1/3 filaments also widens the range in which the device can function.

In addition to facilitating detection of the lowest vibration mode, the bias towards front-end deflection might even bias the overall flapping motion to a lower mode. This would reduce or eliminate the impact of mode transitions on the shape of the frequency-velocity correlation, improving the precision of flow measurement. While this effect hasn't been experimentally tested, consideration of a filament shape with a saturating exponential profile H(x) (figure 6) suggests that it's likely. Such a filament, which would have an extremely thin attachment point H(0) ~=0, would flex solely at the very front end, because the effective flexural rigidity D*H(0) << D*H(x>0). As a result, its flutter would resemble that of a rigid plate freely hinged at the front end, with vibration necessarily constrained to the first mode and described by $f = (p_f U^2/p_s hL)^{1/2}$ [*Mahadevan and Argentina, 2004*]. The flutter of a soft, high-density flag in a low density fluid has previously been described as a resonance of a rigid pivoted plate and a clamped elastic one [*Mahadevan and Argentina, 2004*]. Because a trapezoidal flag of $H_1<<H_2$ approaches the D*H(0)<<D*H(x>0) condition for the flag of figure 6, it's possible that its behavior will more closely mimic that of the hinged plate, effectively constrained to the lowest flutter mode.

Figure 6: *Outline of a flag with a saturating exponential H(x) profile. For such a flag, D*H(0) << D*H(x>0) and the oscillation should resemble that of a rigid plate pivoted at x = 0.*

2.3 Vortex Forcing

A vortex flowmeter uses a bluff body to generate a street of regular vortex structures in dense, high Re, well-developed pipe flows. The frequency of the resulting vortex street is read by a downstream pressure transducer to infer fluid velocity [*R.W. Miller, 1996*]. While the principle of a vortex flowmeter can't be directly extended to a device that operates at very small scales in free air flow, the influence of a bluff body can condition aeroelastic flutter to make it more suitable for wind speed measurement. In particular, the bluff body can provide the 'activation energy' necessary for flutter onset at lower U_C, and can lead to a more-regular flutter frequency – air velocity correlation.

Over the large Re range encountered by an oscillation-based anemometer, vortex shedding in fact occurs in two distinct regimes. In $100<Re<\sim10^4$, vortex structures are shed as $St = fv/d = 0.198(1-19.7/Re)$ (in the case of a cylindrical bluff body). In $10^4<Re<10^6$, distinct vortex structures are difficult to resolve. Above $Re = 10^6$, the vortex structures return in the turbulent regime [*Gerrard, 1966, 1978*].

Eliminating Onset Hysteresis

As speculated in [*Zhang et al., 2009*], hysteresis in the transition to flutter may be explainable in terms of a potential barrier between a filament's stable and fluttering states. This phenomenological description is corroborated by [*Pang, 2010*], who observation that U_C is highly dependent on noise in the oncoming flow, while U_D can be measured consistently regardless of the flow state. One function of a bluff body in an oscillation-based anemometer, then, might be to produce the flow instability that provides the 'activation energy' to initiate flutter consistently at U_D. Figure 7 shows how a transient upstream disturbance can reduce U_C to U_D, inducing stable flutter below the usual critical velocity even after the disturbance is removed.

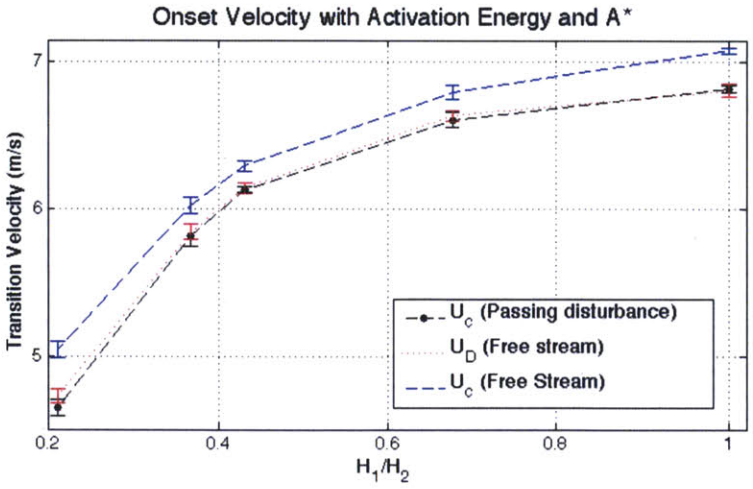

Figure 7: *The minimum upwards critical velocity after a transient upstream disturbance is almost exactly equal to the usual downwards transition velocity U_D. This trend holds for a variety of flag aspect ratios H_1/H_2, all of the same A*. The experiment was performed by experimentally measuring U_D, and testing the minimum velocity of sustained flutter after a transient disturbance of arbitrary magnitude provided the 'activation energy'.*

While the disturbances used to bring U_C down to exactly U_D were too large to be incorporated into an oscillation-based anemometer, the experiment did support the 'activation energy' view as an accurate first-order description of the onset hysteresis phenomenon. Moreover, further experiments with 'fishtail' flags and small bluff bodies showed that there is effectively no hysteresis in the transition to flutter in the event that the bluff body is not removed; in that case, the critical velocity U_{CV} is well below either U_C or U_D. From the data in figure 10, this relationship is approximately $U_{CV} =\sim U_C(1-.8d/L)$ for the range $0<d<L$.

Smoother Flutter with a Vortex Street

As pointed out by [*Manela et al. 2009*], the vortex street shed by a flagpole adds a forcing term to the flag's equation of motion. [*Wang et al. 2009*] asserts that this forcing dominates the filament's motion, based on a soap film experiment conducted with a cylinder of diameter d = 4mm and a filament of L = 10mm and flexural rigidity $D*H = 6*10^{-10}$ Nm^2. However, [*Wang et al. 2009*] conducted frequency measurements at only one velocity, U = 2.0m/s. Experiments at a variety of velocities suggest more complex interactions between the filament and a vortex street.

A nylon flag of L = 8mm and A* = 4, and $D = 9*10^{-5}$ was placed in the wakes of different-sized cylindrical bluff bodies of diameter d. As shown in figure 8, the filament was placed a distance d to the side and d downstream the cylinders, to avoid the potential of reduced local velocity over the flag. The flutter frequency—air velocity correlation of the flag was then measured with a discrete photointerrupt at x = 3L/4.

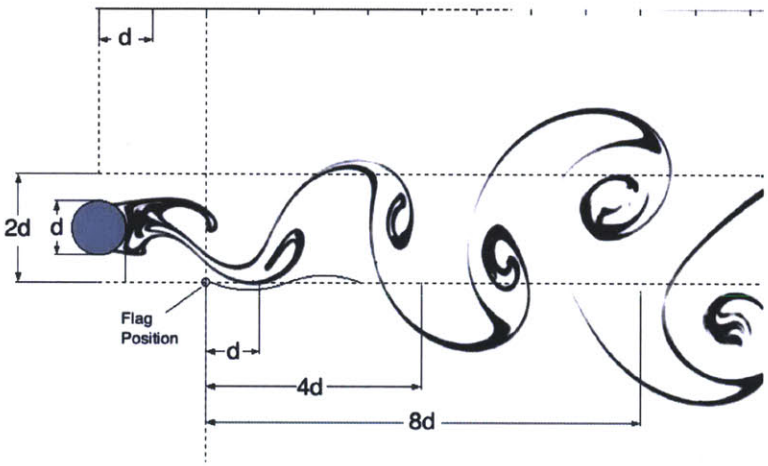

Figure 8: *Placement of the filament in the vortex forcing experiment. Considering only the 2d interactions, the flag should only be expected to oscillate under the influence of one side of the vortex street. Image modified* from [*Van Dyke, 1965*].

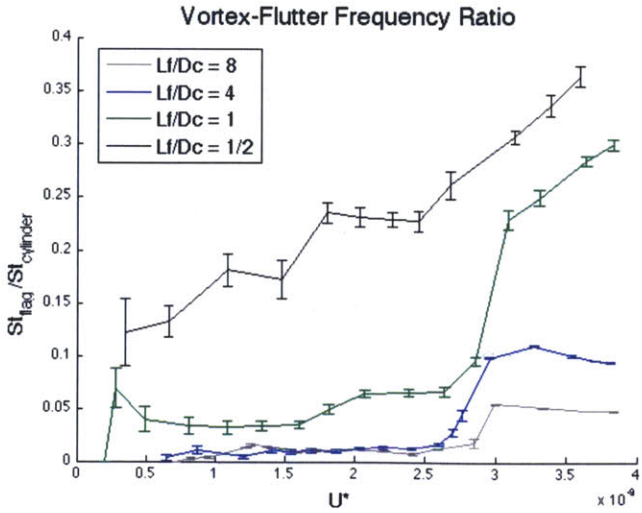

Figure 9: *The ratio of the flag flutter Strouhal number $St_{flag} = f*d/U$ to the vortex shedding frequency $St_{cyl} = 0.198(1-19.7/Re_d)$.*

Clearly, while the flag was influenced by the vortex street, its oscillation stayed well below the vortex frequency, in contrast to the conclusions of [*Wang et al. 2009*]. It is possible that the 2-D flag immediately behind the bluff body impeded vortex formation in these experiments in a way that the effectively 1-D filament's used in [*Wang et al. 2009*] did not. However, the more likely explanation is that behavior of a flag in a vortex street is more complicated than previously described, and likely depends on the flag's stiffness D, the vortex strength, phase relation, and other factors.

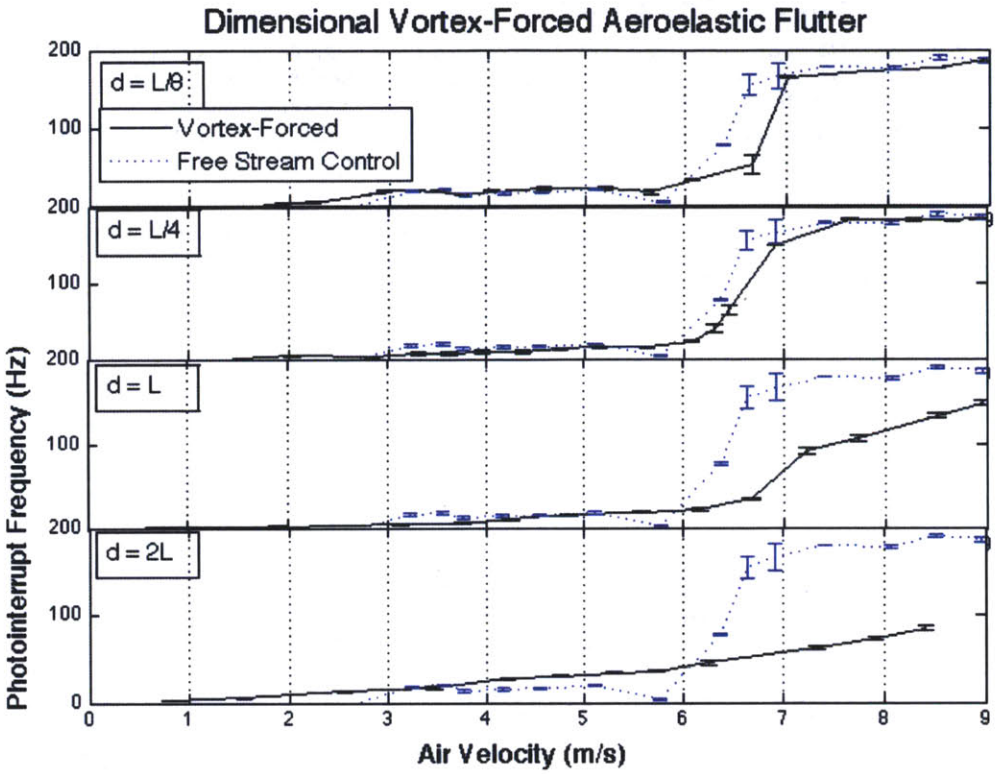

Figure 10: *The data from figure 9 shown in dimensional terms. The dotted blue trace shows the behavior of the same flag in free stream. Clearly, larger vortex structures do more to smooth the flutter and lower U_C than those from smaller bluff bodies.*

For the purposes of an oscillation-based anemometer, the most applicable results are summarized by the representation of the data in figure 10. The larger bluff body does more to influence the flutter behavior, with a monotonic correlation and 80% lower U_C by L=d.

2.4 Filament Material

A filament's composition has a large influence on its flutter behavior. The most important factor is D, which has a large influence on U_C, as shown in figure 11. However, as described by [*Eloy et al., 2009*], the mass ratio M* is also important to keeping the flutter in a lower mode. For the purposes of a practical anemometer system, the primary challenge is to choose a material with as low as possible D and M* that is also as robust as possible, and whose characteristics will not change with time via plastic deformation or fatigue.

To assess the suitability of different materials for use in an oscillation-based anemometer, samples of four plastic films were tested for both onset velocity and flexural rigidity D. Onset velocity was determined by measuring U_D based on the behavior 8mmx8mm rectangular flags. The flexural rigidity D was determined by testing the deflection y(x=L) of longer strips of material under the force of gravity.

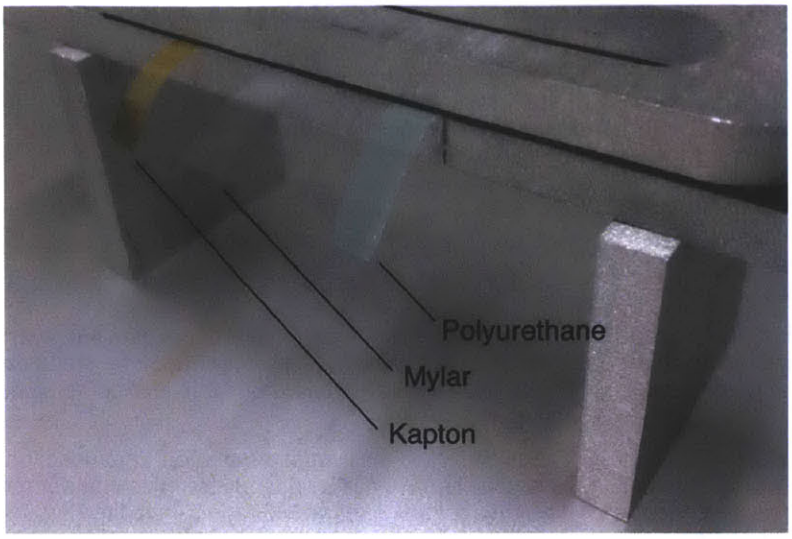

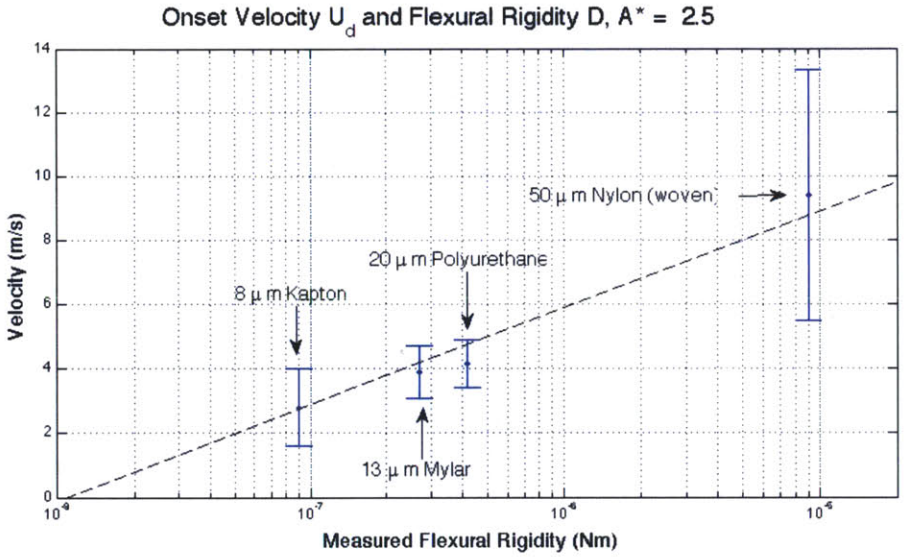

Figure 11: *Kapton is the highest performance material out of several tested. However, the thicker Mylar material, while slightly more rigid, may offer advantages in strength and durability.*

For comparison, the tensile strengths of each of these films are given along with other properties in table 1, below. The last three columns are based on literature values in [*Diaconu et al., 2005*], [*Dupont, 1999, 2006*], [*Kurimoto et al., 2000*], [*Su et al., 2003*].

Table 1: Summary of Measured and Literature Properties of Different Plastic Films

Material	Measured Flexural Rigidity D ($Nm * 10^{-6}$)	Calculated Flexural Rigidity D ($Nm * 10^{-6}$)	Plane Density m (g/m^2)	Tensile Strength T (MPa)
Kapton 8um	0.09	0.096	10	110
Mylar 13um	0.12	0.140	17	178
Polyurethane 20um	0.15	0.07	22	60
Nylon (woven) 50um	8.77	9.12	44	165

Instability at low U is critical to measuring wind speed; if the filament doesn't oscillate, any further effort is futile. Among the four material samples tested here, Kapton was therefore chosen as the best choice film for incorporation in the anemometer due to the low U_D and D. However, it is recognized that both the Mylar and Polyurethane films are also strong candidates. The Mylar film is significantly stronger and also heavier, which is predicted to lead to lower M* and oscillation in a lower mode [*Eloy et al. 2009*]. Moreover, while there was a significant discrepancy between the calculated and measured flexural rigidity D for the Polyurethane film, based on the literature values in [*Su et al., 2003*], Polyurethane could allow a system to work with low onset velocity at very small scales (see section 2.6). For larger (mm-scale) systems, Polyurethane is attractive because the greater material thickness is more conducive to optical edge-detection.

2.5 Nozzle Integration

A working aeroelastic oscillation-based anemometer requires mounting in a protective structure of some kind, as all manner of disturbances—a sudden crosswind, a splash of rain, or a curious toddler—could irreparably damage the oscillating filament. However, mounted in a small tube, the oscillation-based anemometer could be conceivably made far stronger than any comparable device in the sub-centimeter size class.

Depending on the ratio of the tube diameter to the maximum oscillation amplitude, d_{tube}/y_{max}, the tube mounting could significantly interfere with the dynamics of the flag. However, this interference could improve the anemometer operation. In particular, if the tube were structured to cause a local flow acceleration over the flag, oscillation could occur at very low outside velocities even using a filament with $U_C > U_{Outside}$. A nozzle-shaped housing would cause this local flow acceleration, and its integration into an aeroelastic oscillation-based anemometer is depicted in figure 12.

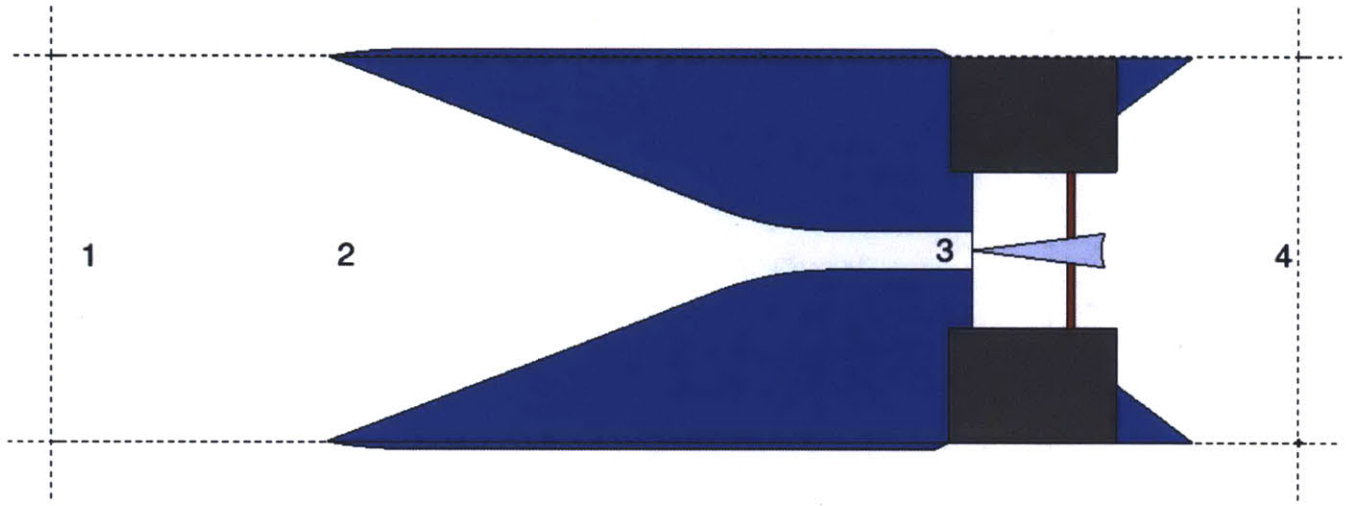

Figure 12: *Schematic of a nozzle-integrated prototype. Free-stream air at point 1 enters the system at point 2, accelerates over a 'fishtail' filament attached at point 3, and exits at point 4. A photointerrupt laser is shown recording the flutter of the filament between points 3 and 4.*

When air in a duct passes through a nozzle, the local acceleration is easy to calculate based on the first and second laws. In the case of an inviscid, incompressible fluid that applies to the anemometer, as Ma > 0.1, this simplifies to $U_3 = U_1*(A_2/A_3)$, where A_n is the cross-sectional area of the nozzle at point n shown in the figure. However, the case of a nozzle in free flow is less clear-cut. Friction through the nozzle results in a back-pressure at point 2 which will reduce flow through the nozzle, reducing U_3.

While not very satisfying theoretically, one way to describe the performance of nozzles is with a pressure recovery factor, $Eta = (U_{3,A}^2 - U_1^2)/ (U_{3,P}^2 - U_1^2)$, where A and P indicate actual and projected figures, respectively. Experiments on a variety of nozzle geometries (shown in figure 13) were performed by measuring the stagnation pressure at point 3 in a range of wind tunnel velocities. The nozzle velocity $U_{3,A}$ was then calculated by the Bernoulli equation along the streamline from point 3 to the flag position, which is assumed to be at the ambient pressure.

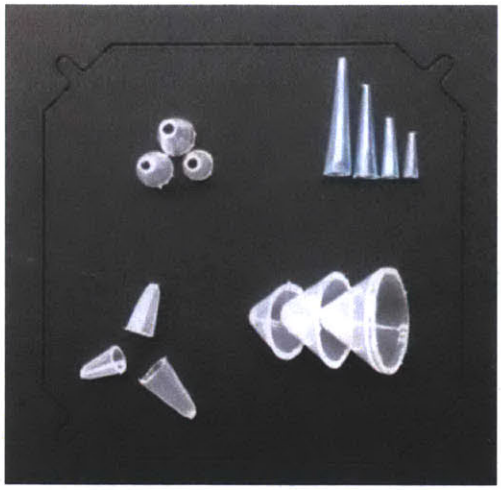

Figure 13: *Nozzles of linear profile and different slopes were tested, each at three different lengths and with the same throat (point 3 in figure 12) diameter.*

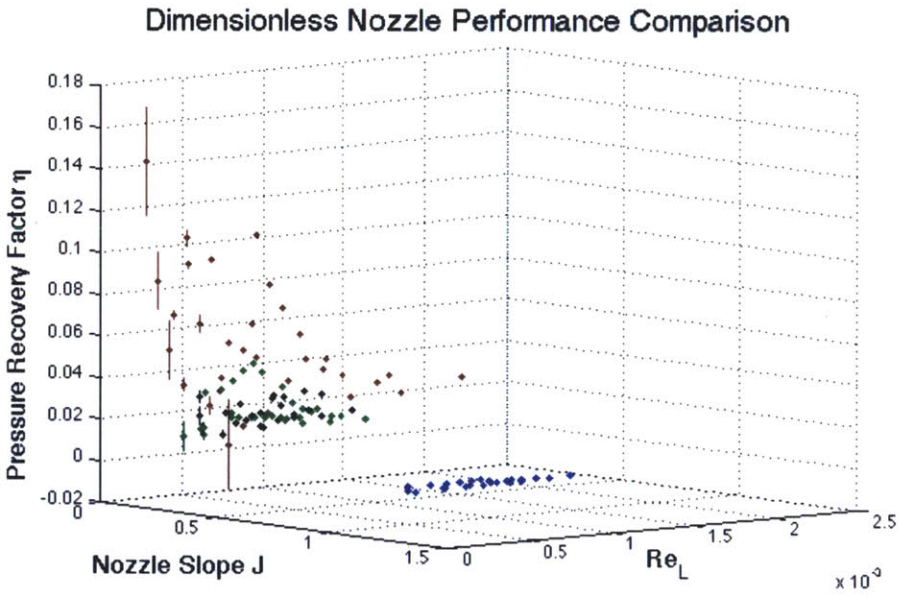

Figure 14: *Performance of various linear nozzles in terms of the throat Re and wall slope. In dimensional terms, because of the greater ratio $U_3 = U_1*(A_2/A_3)$, performance did not vary significantly with the overall geometry.*

Based on the data presented in figure 13, the performance of linear nozzles in free stream was uniformly poor and varied as eta= $.08/(J+1)^2$, where J is the nozzle slope $(d_1-d_3)/L$.

An iterative approach to modeling flow through the nozzle was also formulated. It involved several steps:

1) Assume continuity between points 1 and 3 to make an initial guess of U3 =A1U1/A3.
2) Use energy conservation (Bernoulli) on the streamline 2-3 to find the throat pressure P3.
3) Use Darcy's law to estimate non-conservative pressure loss between P2 and P3, using a lumped frictional loss coefficient K= 0.1 3) Use energy conservation on the streamline 1-2 to re-estimated the inlet velocity V2.
4) Use continuity between points 1 and 3 to refine the initial estimate, now using the inlet velocity U3 = U3 =A2U2/A3.
5) Iterate steps 2-4 until the output U3 stabilizes.

While this approach gave good results for K = 0.1, it relied equally on an empirically-derived constant, and was less simple to implement. As a result, the empirical pressure recovery factor was used to rate prospective nozzles for the anemometer system.

2.6 Scaling Limits

A main attraction of the aeroelastic oscillation-based anemometer concept is that there are few challenges in manufacturing the device at very small scales, in contrast to traditional rotary encoder or pressure transduction-based flowmeters. From a fabrication standpoint, aeroelasticity-based fluid measurement should therefore be possible even on the MEMS scale. To investigate this possibility, it's necessary to investigate the scaling limits of both purely aeroelastic and vortex-coupled anemometer systems.

Re limits the miniaturization of a vortex-forced system. Although bluff bodies produce oscillatory flow from Re ≈ 35 [*Gerard, 1978*], Re ≈ 100 is the lower limit for vortex-forced flutter [*Manela, 2009*]. A system designed to work in air above 5m/s would require a bluff body with a characteristic length of at least 0.33mm. Given the minimum effective ratio $D_c/L_f \approx 0.5$ suggested by figure 2, the smallest possible flag-coupled vortex-driven system would be ~0.7mm for these conditions.

In contrast, aeroelastic flutter does not seem to be subject to a minimum Re. Scaling factors proposed by [*Bao, 2008*] and [*Zhu et al., 2002*] predict the onset of flutter to be dependent only on flag material and geometry. The dimensional predictions in [*Argentina et al., 2004*] for U_c and initial frequency f echo this:

$$U_C \sim (Eh^3/p_fL^3)^{1/2} \quad f \sim (p_fU_C^2/m)^{1/2}$$

The lesson of these scaling factors is that, while not limited by a strict Re cutoff, the practical lower limit of flow measurement based on aeroelastic flutter depends on the minimum manufacturable ratio h/L and the elasticity E. Practically, this means that the feasibility of truly micro-scale oscillation based anemometer depends on the materials used; based on the free-stream onset data of figure 4 and the relations above, a rectangular Polyurethane filament with L = 50um would need to be manufactured with a thickness in the tenths of microns in order to function as a micro-scale aeroelastic anemometer. The scaling estimate is shown for a range of L and U_C in figure 15. The maximum material thickness would likely be significantly greater for a 'fishtail' shape flag, as described in section 2.2.

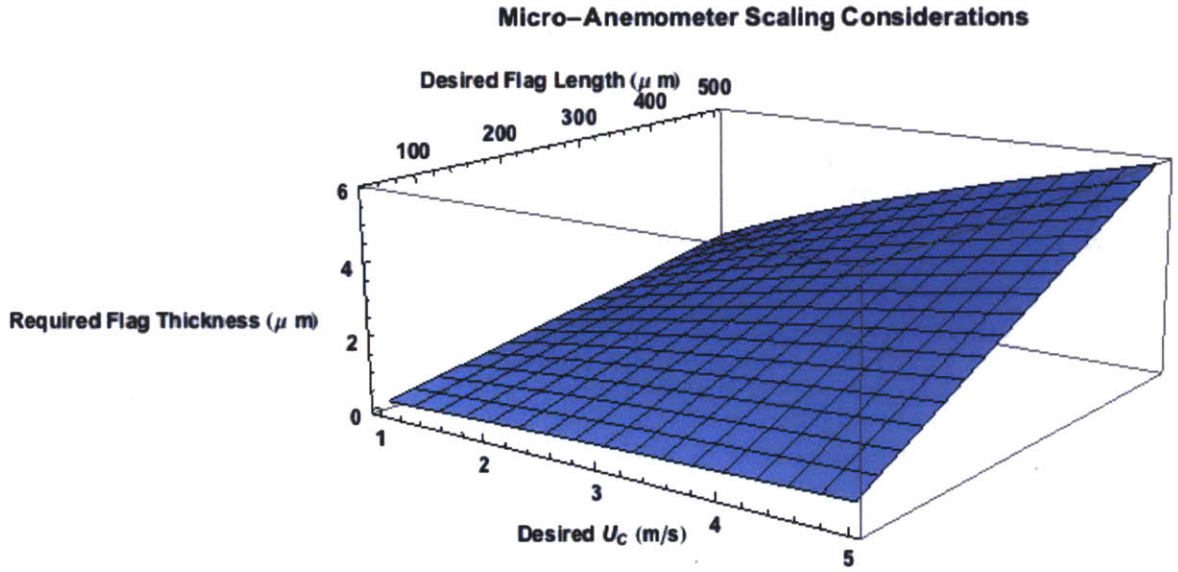

Figure 15: *The flag thickness required to measure flow via oscillation at a given scale L and with a given U_C, based on the scaling factors proposed by [Argentina et al., 2004], and the data presented in figure 4.*

Clearly, while a micro-scale anemometer is not outside of the realm of possibility, manufacturing a sub-micron plastic film is outside of the scope of this work. With macro-scale fabrication techniques, the smallest effective aeroelastic oscillator produced in this effort was a 'fishtail' shaped unit with L = 2.95mm and H_2 = 0.7mm. It was made of 20um polyurethance and attached a 'flagpole' of carbon fibers with contact epoxy as shown in figure 16. This filament still operated in the vortex-forced regime; its frequency-velocity correlation when coupled to a d= 0.8mm bluff body is shown in figure 17.

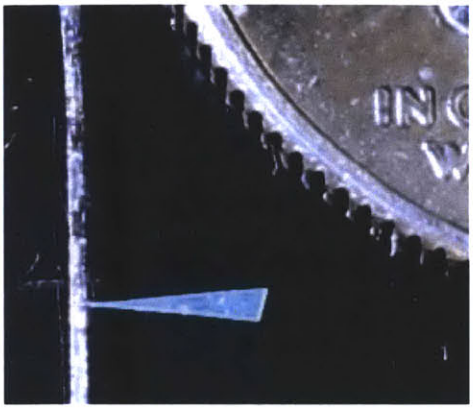

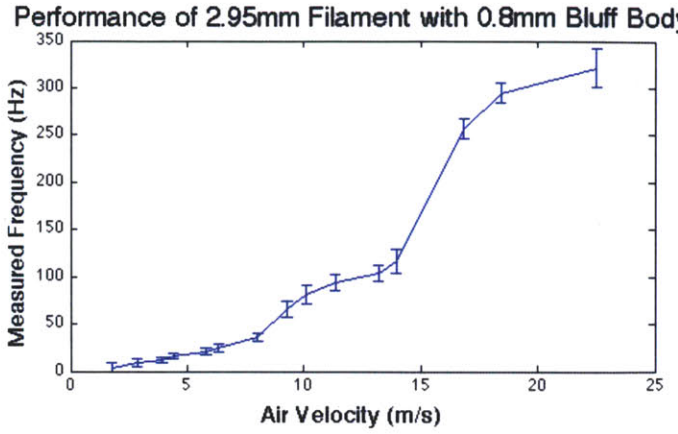

***Figures 16 and 17**: An ~3mm polyurethane filament shown near the edge of a US dime, and its performance correlation from 2-22m/s.*

Interestingly, the size of the vortex-coupled system shown here was primarily limited by the resolution of the photointerrupt detector strategy, not any flutter law. As is clear from figure 17, this particular geometry could not have been further minimized without suffering an increase in U_C beyond 2m/s. However, this issue does illuminate another advantage of the fishtail filament shape; given that some twisting of the filament is likely during flutter, the fishtail's relatively large rear area is far more detectable than that of a rectangular filament with comparable D.

2.7 Second Onset Velocity

As shown in figure 2, flags in free stream have frequency-velocity correlations that show a series of prominent 'bumps'. Furthermore, while the individual correlations differ, flags of different A* all show a distinct frequency dip at U =~$1.5U_C$. This trend is also shown in both the free-stream and vortex-forced data in figure 9.

While more experiments would need to be conducted to produce a definitive result, the dip in frequency near U* =~$3U_C$* could be related to the "second critical velocity" predicted by both [*Pang, 2010*] and [*Eloy, 2009*], but not observed experimentally thus far. The two U_C values for each flags would fit the form of their onset collections, slightly offset on the graph of m* vs. U_C*, as in figure 18, below.

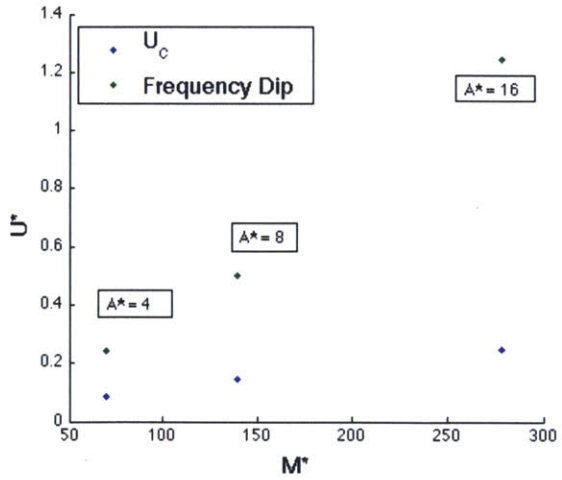

***Figure 18:** Possible locations of the "fold over" in the criticality graph of [Eloy, 2009], pinpointed not as a second critical velocity but as a frequency minimum at approximately U = 3 U_C.*

3. Prototype Design

This research on aeroelasticity-based flow rate measurement informed the design of a compact, robust anemometer prototype that reliably measures air flow over a 24m/s range. While this system is far more reliable than previous proof-of-concept efforts (described in section 6.1) it still lacks some of the design finesse and systems integrations of a possible commercial system. This section describes the selection of the filament shape and sensor strategy, and details the prototype's electrical, mechanical, and software characteristics.

3.1 Experimental Design Optimization

The observations of section 2 inform the design of a mm-scale prototype in several ways. These implications can be summarized separately in terms of filament optimization, bluff-body coupling, and nozzle integration.

Optimizing the Filament for Durability and Instability

The ideal filament has a combination of effective rigidity Dh and geometric parameters A* and H_2/H_1 that give it a very low U_C without making it too fragile. The optimization begins by clarifying the tolerable combinations of these three factors with regards to filament strength, and then explores the most advantageous combinations based on the experimental relationship from section 2.1: U*~1.1+.15*log(.6*H_1/L)+.05*log(H_2/L) and [*Argentina et al., 2004*]'s scaling factor for U_C with filament thickness $U_C \sim (Eh^3/p_fL^3)^{1/2}$.

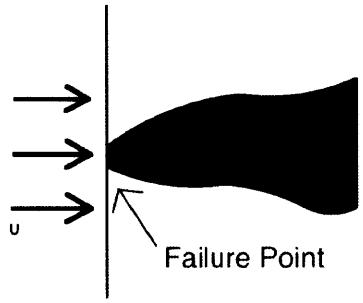

Figure 19: *The front-end of fishtail-shaped filaments is the most common failure point, and is the focus of the tensile loading analysis here.*

Both drag and inertial forces must be considered in calculating the expected load on the filament's front end. Assuming an effectively 2-d filament, the force from the passing air can be calculated based on turbulent boundary-layer theory [*White, 2008*].

$$F_{Drag} = \frac{0.31\rho_f U^2(\frac{H_1+H_2}{2})L}{\mathrm{Re}_L^{1/7}}$$

The inertial force is the result of the body of the flag snapping to the rear position after a full swing. For this analysis, the flag is modeled as a pivoted rigid triangular plate oscillating at a worst case amplitude of $theta_{max}$ = pi/2. The inertial force at the midpoint of the swing simplifies to $F_{inertia} = 2(mS)\pi f$. To first order, the total maximum force on the flag is then:

$$F_{\max} = F_{inertia} + F_{Drag} = 2(mS)\pi f + \frac{0.31\rho_f U^2(\frac{H_1+H_2}{2})L}{\mathrm{Re}_L^{1/7}}.$$

Balancing this anticipated load with the tensile strength of the flag front, TH_1h, yields the following relationship between tolerable filament thickness h and flag geometric ratios H_1/L and H_2/L.

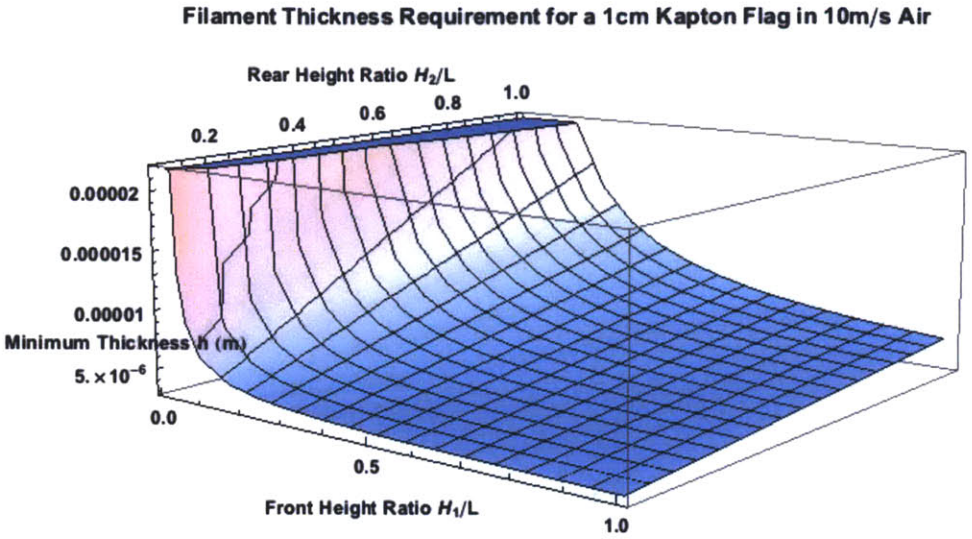

Figure 20: *A conservative estimate of the minimum thickness of a 1cm long Kapton filament in a 10m/s wind as a function of the filament's geometry, based on a tensile strength analysis.*

The immediate conclusion from the analysis of figure 20 is that, on the basis of instability and strength, a large aspect ratio A* (here taken as H_2/L) is always favorable, because it decreases both the onset velocity U_C and the maximum predicted forces on the filament. Of course this must be balanced with the device structure and the desire not to increase the primary vibration mode by increasing M*.

Because the onset velocity has a cubic dependence on the filament thickness, but only a logarithmic dependence on the ratio H_1/L, the priority is to decrease the ratio H_1/L only until the 'knee' point in figure 20 would necessitate increasing the thickness H substantially. For the flag simulated above, that optimization point is near h = 4um and $H_1/L = 0.2$.

The procedure for optimization of the total filament shape is necessarily iterative. With the material choice, h, or A* constrained by the design of a device, the other parameters can be optimized based on the strength analysis presented above and the two relationships given for U_C. This is the procedure that was followed for the working prototype described in section 3.3.

Bluff Body and Nozzle Integration

The optimization of the bluff body and nozzle configuration is less involved that that the optimization of filament shape, so long as the nozzle throat's possible impact on the flag's amplitude is disregarded. The optimization of a bluff body, as investigated in section 2.3, is simple: the bluff body should be as large as possible without impeding flow through the system. The choice of a nozzle shape (assuming a system as shown in figure 21) is constrained by the desired system dimensions and flag size.

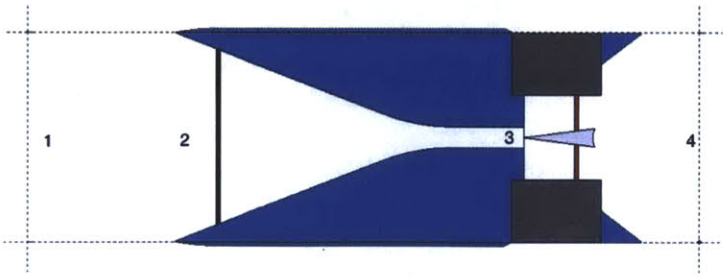

Figure 21: *A conceptual schematic of a nozzle-integrated anemometer system with a bluff body between points 2 and 3.*

To optimize the nozzle and bluff body size, the basic analysis of section 2.5 was repeated, but with $U_3 = U_1*((A_2-A_B)/A_3)$, where A_B is the cross-sectional area of a bluff body shape. In optimizing for instability, this was compared with the experimental correlation $U_{CV} =\sim U_C(1-.8d/L)$ from section 2.3.

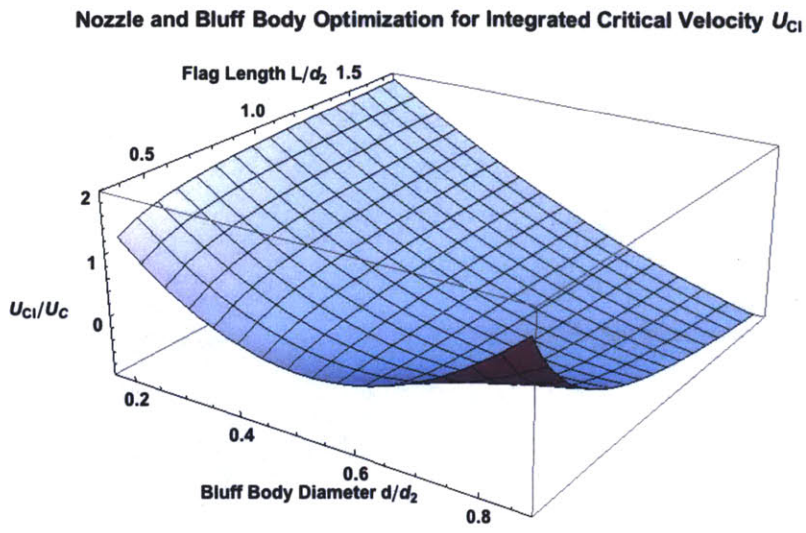

***Figure 22**: The optimum integrated system. Dimension d_2 is the diameter at point 2 in figure 21. Clearly, the optimum bluff body is ~ $0.45d_2$ for short flags.*

3.2 Flutter Detection

There are numerous possibly ways to detect the flutter of a small filament. In this investigation, five types of sensors were analyzed and tested: Piezoelectric pressure transducers, potentiometric displacement transducers, optical rangefinders, and IR laser photointerrupt detectors with both transistor-type and discrete outputs.

Of these methods, three were discarded after only qualitative testing. Both piezoelectric and potentiometric sensors required direct integration into the oscillating filament, as shown in figure 23. This integration compromised the low flexural rigidity that's critical to flutter, and so these sensors were abandoned. The optical rangefinder (figure 23) method also was quickly discarded due to slow response time, although it's likely that this technique could give good results with a different rangefinder and system configuration.

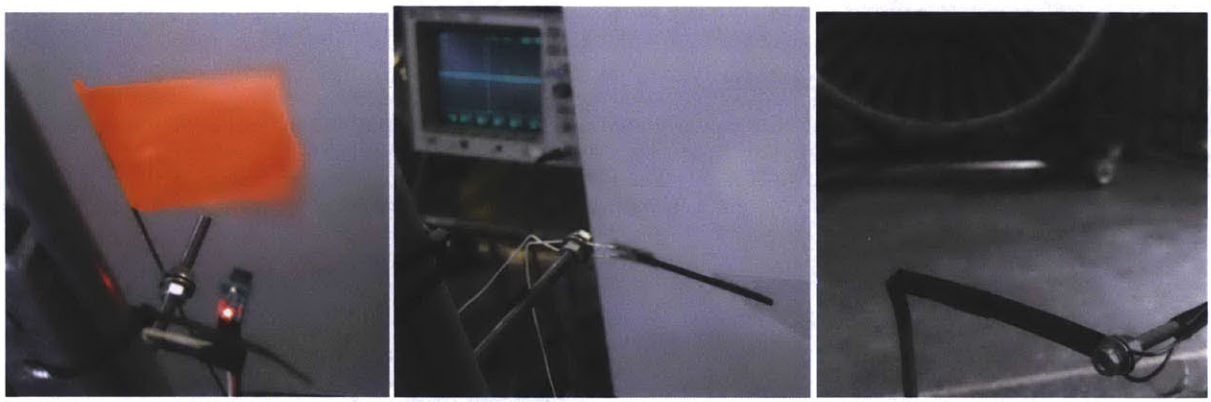

***Figure 23:** From left to right, optical rangefinder, piezoelectric, and potentiometric sensing units integrated in early flutter tests.*

By contrast, the photointerrupt sensors are simple, low cost, and very conducive to system miniaturization. Discrete systems have the benefit of simplifying circuit design, and, if a microcontroller signal processing unit is integrated, the ability to estimate both the frequency and amplitude of flutter by timing both rising and falling edges. This works because the photointerrupt transit time gives the approximate mid-span transverse velocity of the flag, which can be combined with the non-interrupt time and an assumed velocity profile to yield the likely distance traveled.

Analog photointerrupt systems, while requiring either discretization or FFT/DFT processing, can be amplified to measure the flutter of far thinner flags that would be below the resolution of economical discrete units. Due to these different advantages, discrete photointerrupt sensors were used in the larger-scale proof-of-concept prototype described in section 6.1, as well as in most of the tests. Analog sensors were used in the tests of very small filaments and in the system prototype in sections 2.5 and 3.3.

3.3 A Working Prototype

A prototype aeroelastic anemometer was designed based on the analysis of section 2, with the basic nozzle-integrated layout shown in figure 21 in section 3.1. While lacking much of the systems integration of the proof-of-concept design (Section 6.1), this form of the device could be adapted to a commercial system with no fundamental modifications.

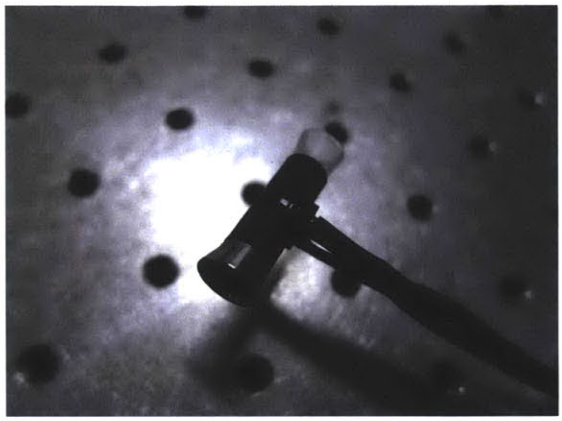

Figure 24: *The prototype. Air flows into the plastic nozzle at the top right and exits through the diffuser at the bottom left.*

Mechanical Plant

A Kapton filament with L = 4mm, h = 8um, $H_2/H_1 =\sim 10$ and $A^* =\sim 10$ were mounted in a tube as shown in figures 24 and 25. The nozzle chosen had a slope J = 0.4 and an integrated rectangular bluff body with $W = L/3 =\sim d_2/2$. The filament was attached to a carbon strand at the nozzle throat with cyanoacrylate glue and allowed to swing in the path of a 2mm-gap slot-type photointerrupt sensor. The filament plane was aligned with the axis of the bluff body and carbon strand, both of which were oriented at an angle of 10° to the photointerrupt beam. This small offset aided detection of the flag motion by presenting slightly more filament material to occlude the photointerrupt beam.

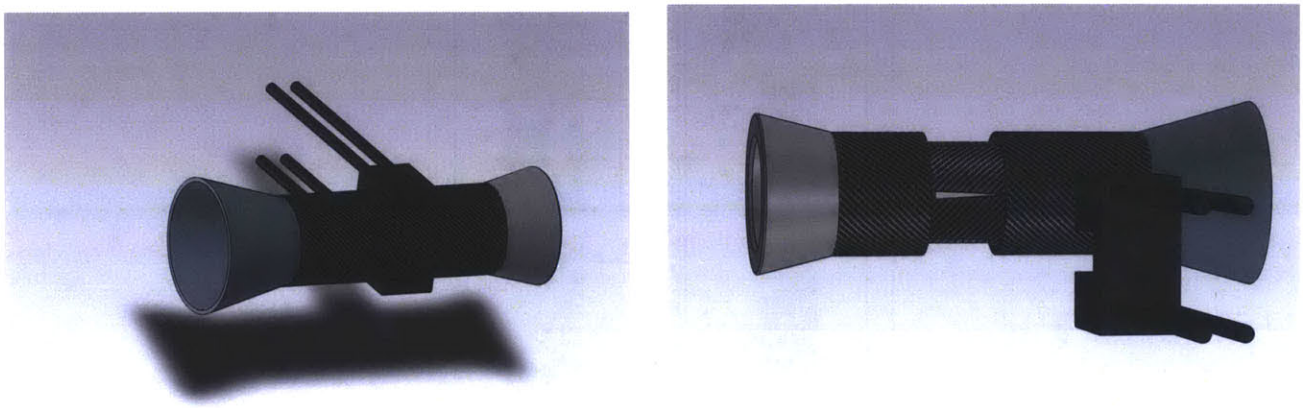

Figure 25: *CAD Assembly of the nozzle-integrated prototype. The filament's attachment to the nozzle is visible when the photointerrupt sensor is removed.*

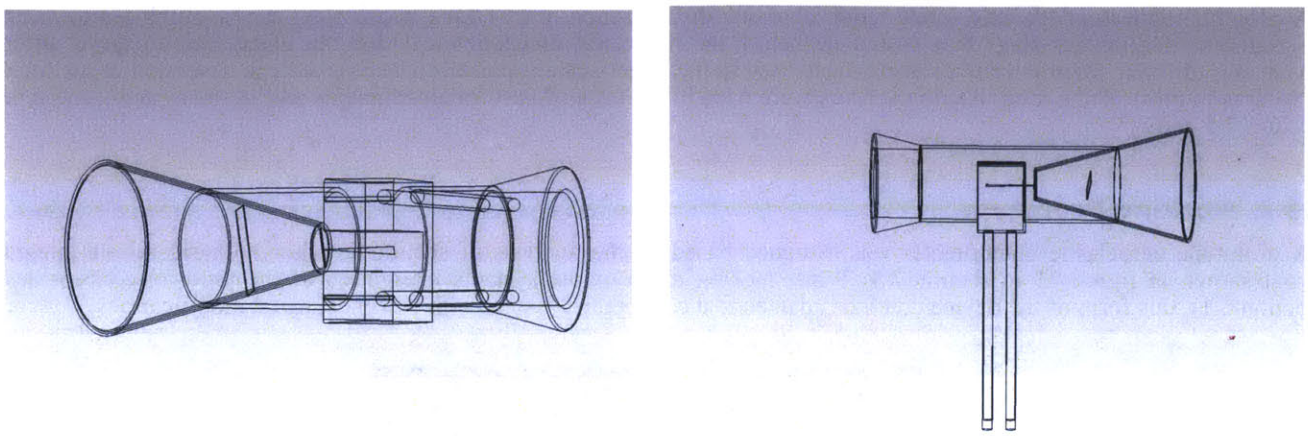

Figure 26: CAD cross section.

Electrical Plant

In contrast to the proof-of-concept system of section 6.1, the electronics plant of this prototype was based on a development board. While it will require substantial redesign for a small-scale PCB implementation, the board allowed rapid experimentation with different signal processing strategies and an easy link with a PC for post processing.

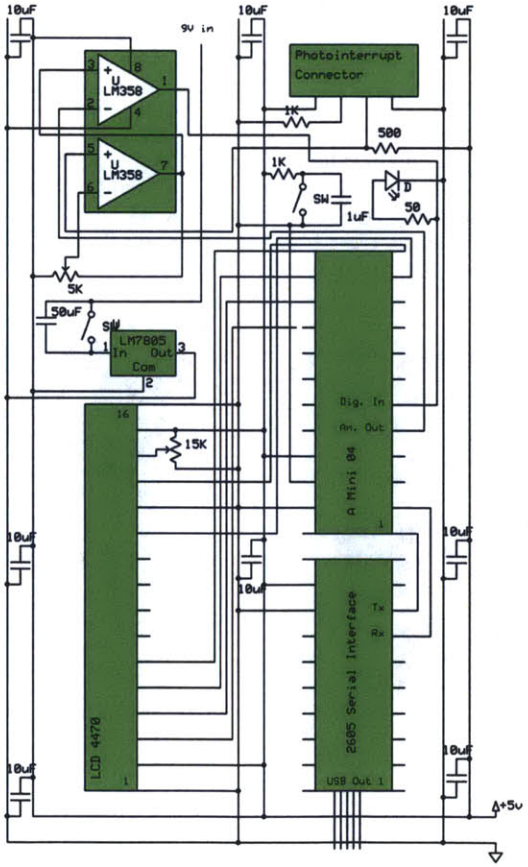

Figure 27: Electrical Schematic of the anemometer system.

Software

The phototransistor output must be amplified for the system to register the passage of the 8um Kapton filament. The appropriate level of amplification depends on the flutter behavior; at low frequencies and low amplitudes, the filament spends enough time in the beam that relatively little (~3x) amplification will result in a detectable signal. More amplification and the sensor will register a constant high level. However, at higher frequencies and amplitudes, far more (~9-15x) amplification is required to detect the passage of the filament. Controlling the signal amplification level, then, requires some intervention from the microcontroller.

This prototype uses a 'perturb and observe' algorithm to resolve this problem. As shown in figure 28, below, the controller periodically interrupts the ordinary cycle of edge counting and output to adjust both the gain and discretization level. If the adjustment results in a higher input frequency, the current measurement series is overwritten with measurements taken at the 'correct' gain level. This system could have been implemented by manipulating the power delivered to the photointerrupt IR laser, rather than the signal gain. While this strategy may have given slightly quicker results, the risk of accidentally overdriving the LED outweighs the potential benefits.

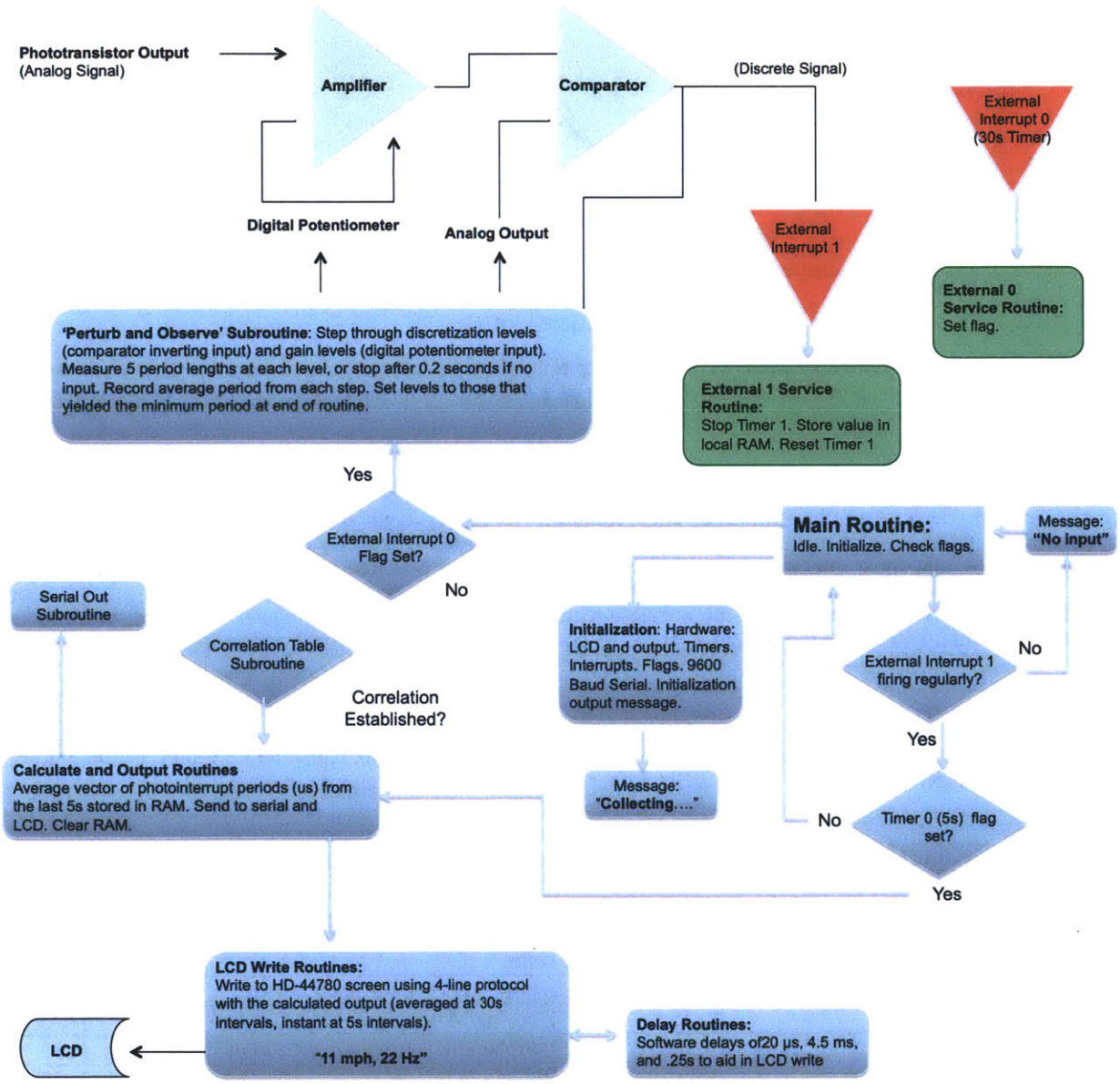

Figure 28: *Anemometer microcontroller software flowchart including the 'perturb and observe' subroutines.*

Performance

The prototype indicates air velocity repeatably from 1-25m/s. Below that range there is no detectable oscillation. Above that range the filament attachment may break. While no system has been made with a hard-coded correlation for final performance testing, the unit's frequency-velocity correlation for three separate tests is shown in figure 29.

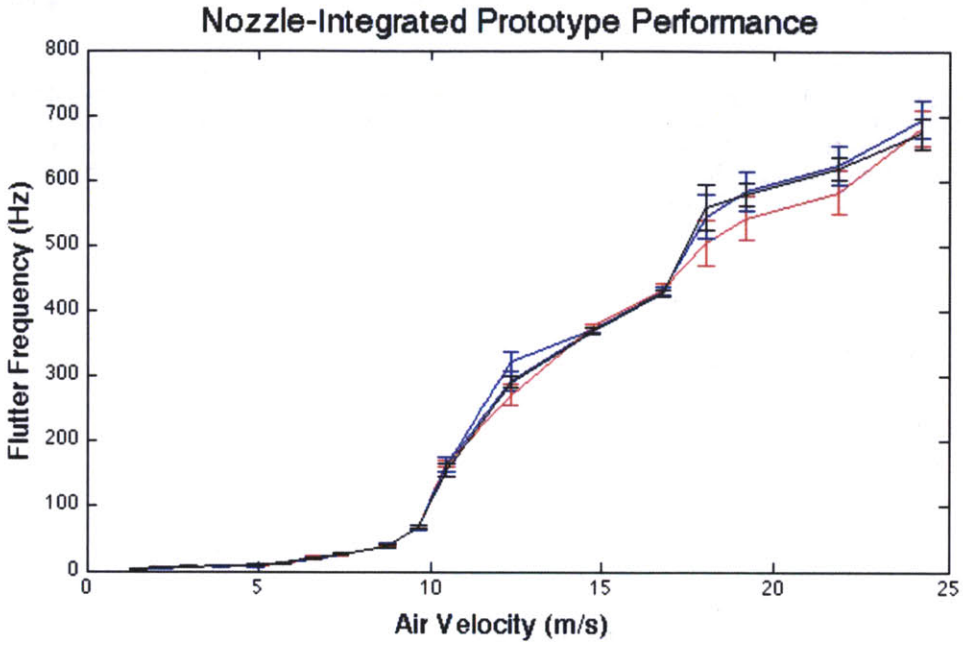

Figure 29: *The air velocity—flutter frequency correlation of the prototype, developed over three tests (shown here as red, blue and black traces). The device has an expected accuracy of ±0.5m/s to 18 m/s, and ±2m/s above. These figures can likely be improved by averaging over a greater collection time.*

While the performance and reliability of this system vastly exceed that of the proof-of-concept prototype (section 6.1), it is worse in one respect. Because of the primitive 'edge counting' frequency method implemented, the system has a slow response time; it must wait several seconds between measurements in order to properly calculate the frequency. This isn't a large drawback, given that most anemometers only report data at 30- or 60s intervals. However, many of the potential applications for a micro-scale flowmeter may require a faster response time. A slightly more powerful processor or more agile software could likely interface to the same nozzle-integrated mechanical plant. By measuring pulse width rather than edge count, this controller could give the system a <0.25s response time for the full velocity range.

System Cost

Table 2, below shows the cost of both the actual prototype system and an equivalent system using a lower-cost microcontroller with simple serial output and no LCD, rather than a full development kit.

Table 2: Prototype cost breakdown. Clearly, costs would be reduced if items were purchased in bulk.

Actual Prototype		**PIC-Microcontroller Implementation**	
Item	**Cost ($)**	**Item**	**Cost ($)**
Sharp™ Photointerrupt	1.58	Sharp™ Photointerrupt	1.58
Housing Materials	.75	Housing Materials	.75
Peripheral ICs (op-amps etc.)	.10	Peripheral ICs (op-amp, crystal etc.)	.30
Amini uC	35	PIC uC	.50
Amini USB interface	20	7805 Power regulator	.10
Hitachi 4470 LCD	12	DAC IC	.35
Passive Components (Resistors, Switches etc.)	.40	Passive Components (Resistors, Switches etc.)	.60
Total:	69.83	**Total:**	4.13

4. Discussion

The aeroelastic oscillation-based anemometer could potentially be developed into a low-cost flow measurement system for a variety of applications. This section discusses future improvements to the prototype, compares it with available anemometer systems, and explores realistic commercialization prospects.

4.1 Future Improvements

Several very basic improvements could potentially increase the effectiveness to the prototype presented in section 3.3. These include modifications to the mechanical, electrical, and software plants.

While the linear nozzle profile clearly contributes to flow acceleration over the filament, parabolic nozzle and diffuser sections would likely enhance this effect [*R.W. Miller, 1996*]. Because the performance of the device is limited more by the size of the filament than the housing, the entire mechanical plant could be further miniaturized to maximize the size of the filament relative the entire device. The filamen attachment would be strengthened and weatherproofing added outside the photointerrupt sensor slot to enhance durability. Additionally, in a future PCB implementation the entire electrical plant could be mounted directly on the prototype. These improvements to the mechanical plant are summarized in the conceptual drawing of figure 30, below.

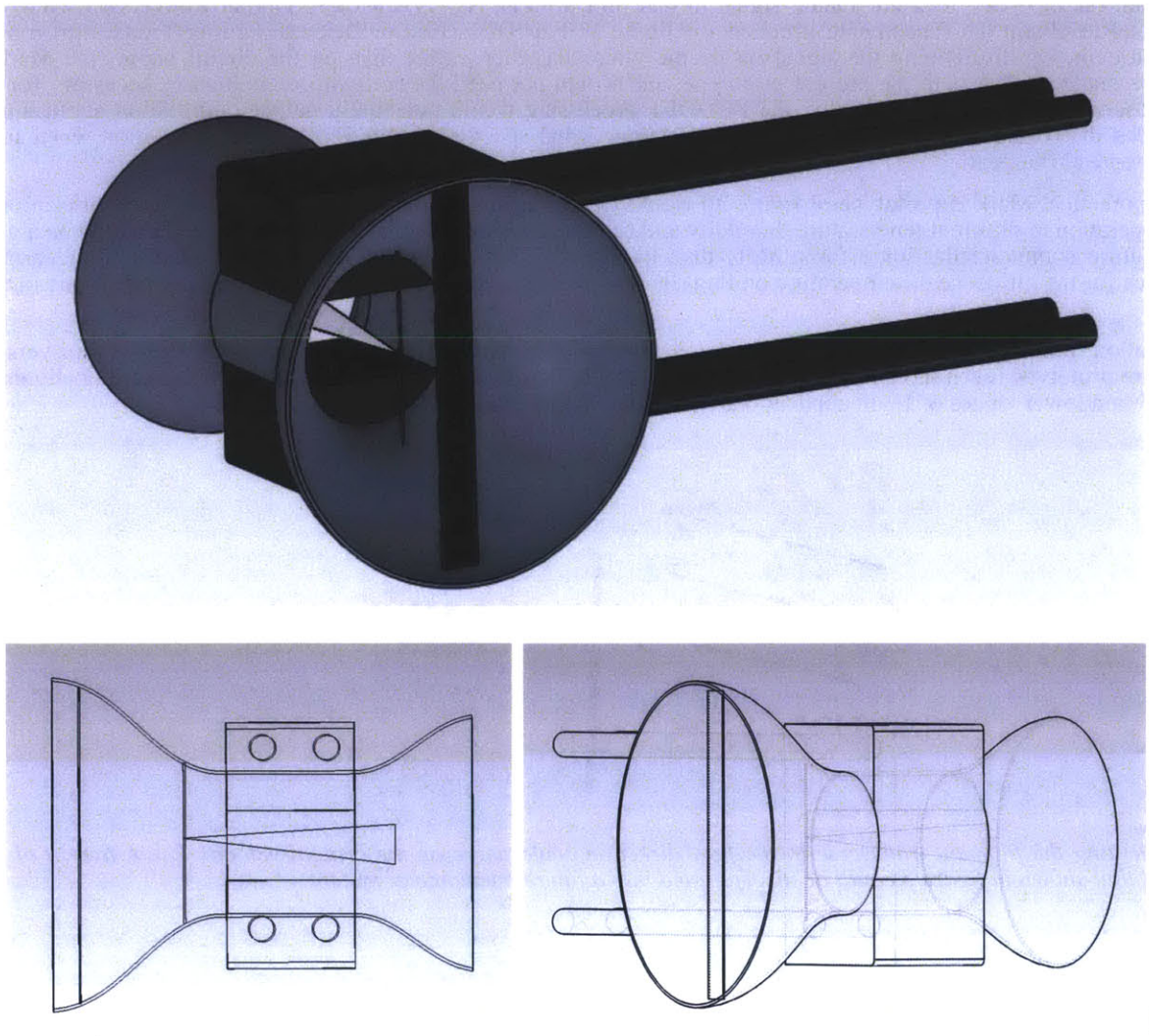

***Figure 30**: CAD rendering of a hypothetical Mark-II prototype.*

Table 3: Cost Breakdown of the Mark-II prototype shown in figure 30

Item	Cost ($)
Sharp™ Photointerrupt	1.58
Housing Materials	.75
Peripheral ICs (crystal etc.)	.30
PIC uC	.50
7805 Power regulator	.10
ADC IC	.95
Passive Components (Resistors, Switches etc.)	.40
Electronics housing and PCB	1.00
Weatherproofing Silicone	.05
USB Output Connector	1.00
Total:	6.33

A Mark-II prototype would also benefit from a more-agile data processing routine. While the 'perturb and observe' algorithm is an effective use of limited processor resources, a more advanced strategy would be to amplify the phototransitor output by a small factor (~2x), read the analog signal in real time with an ADC (Analog-to Digital Conversion) chip, and process the signal to obtain the fundamental frequency with an FFT or DFT (Fast or Discrete Fourier Transform) routine implemented on-chip. By discretizing the signal inside the microcontroller, rather than on the circuit board, the Mark II system could be made smaller than the present prototype, and would not need the constant re-calibration necessary for the 'perturb and observe' prototype. Additionally, the FFT/DFT processing would potentially gather information about higher oscillation modes that could be used to create a more accurate wind speed-photointerrupt output correlation, even for a substantially non-ideal filament.

While the hypothetical Mark-II prototype of figure 30 would clearly have to undergo far more testing and optimization to assure proper operation in different temperature, humidity and turbulence conditions, this form of the device would be a good candidate for future commercialization efforts. More than likely, other sub-systems (such as a temperature compensation circuit to balance for the influence of temperature on flag rigidity) would have to be implemented in the course of this further development.

A last observation from filament testing was that many filaments will oscillate at lower U_C when the air flow is transverse to the flag. A future prototype (even more advanced than that shown in figure 30) could use a slightly transverse flag alignment (figure 31) to obtain lower values of U_C in applications where that is necessary.

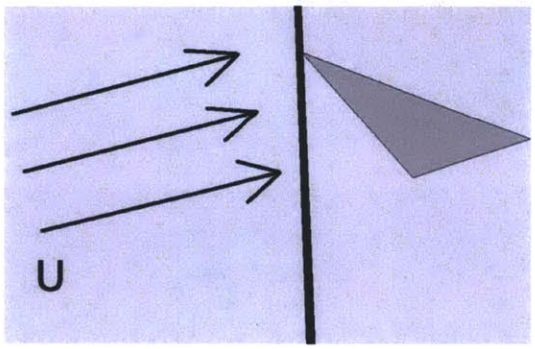

Figure 31: *Orienting the filament transverse to the flow direction could decrease the critical velocity U_C. A hybrid of this orientation and that shown in figure 3 could be incorporated into a future anemometer system.*

4.2 Performance Comparison with Available Anemometers

Table 4 shows the performance and size of several other low-cost flowmeters with which the oscillation-based anemometer could conceivably compete commercially.

Table 4: Specifications of the lowest-cost options from four leading anemometer manufacturers compared to the prototype aeroelastic system[1].

Anemometer Model	Type	Dimensions L x W x H (cm)	Accuracy (m/s)	Range (m/s)	Cost ($)	Other Features
NRG Systems #40H	Rotary (Hall Effect)	5.1x5.1x8.1	0.1-0.45	1-96	175	None
SmartSensor AR816	Vane (Hall Effect)	4x1.5x10	0.5-1.5	0.3-30	50	Temp.
General Tools WS821	Rotary (Optical)	10x6x4	0.5-2	0.5-89	199	Temp.
Extech 45118	Vane	13 x 7 x 1.9	0.2-1.5	0.5-28	109	Temp.
*Aeroelastic Prototype	Aeroelastic Flutter	2 x 0.5 x 0.3	0.5-2	1-25	4	None

Clearly, the prototype anemometer of section 3.3 offers performance that is comparable only to the lowest-end models from the leading manufacturers. However, this does not factor in likely performance improvements that would come with a Mark-II prototype. Additionally, the aeroelastic system offers distinct advantages in both cost (less than 10% of the nearest competitor) and size (volume less than 0.5% that of the nearest competitor without electronic integration) that could make it preferable for many applications.

4.3 Niches and Commercialization:

A streamlined Mark II prototype as presented in section 4.1 (figure 30) could compete with the traditional anemometers of table 4 in a range of typical anemometer applications, including wind resource assessment, meteorological studies, environmental monitoring, sailing applications and wind turbine control, so long as the filament were adequately protected from blowing rain. However, the small size and low cost of the system also make it a candidate for other flow measurement situations that may be unsuitable for other anemometers. Possible applications include measuring air flow within the ducts of HVAC systems, inside intake pipes for vehicles, or serving as a speedometer on low speed unmanned aerial vehicles (UAVs) such as remote-controlled helicopters. In the HVAC system application, the aeroelastic anemometer could serve as an ideal 'limit switch' to monitor air flow levels in different parts of the system. In the context of wind resource assessment, the low cost of the anemometer could make it ideal for creating large 3-d arrays to determine the ideal turbine position without disturbing the nearby flow. A network of the aeroelastic anemometers could even be mounted on a turbine blade to provide a real-time indication of the flow pattern over the blade and help refine the blade design. In a meteorological application, the low-cost and light weight of the anemometer would make it ideal as a disposable wind speed meter to be mounted on a weather balloon. Clearly, the extreme low cost and scaleability of the system open up many applications unsuitable to larger and more expensive traditional anemometers.

Possible Conflicts with Prior Art

Two U.S. Patents have been already been issued for oscillation-based anemometers. Issued in 1966 and 1987, both describe large, rigid, hinged structures that rely on lift forces and inertial overshoot to create a sustained oscillation in strong winds. The patents give only analytical guesses for the flutter frequency-wind velocity correlation that is expected, and neither mentions a practical method for measuring the output oscillation; most likely, no prototypes were built. Moreover, it is evident from the limited analyses presented that both devices would only oscillate in a narrow wind speed range. Neither is realistic competition, either commercially or in an intellectual property sense, with the mm-scale aeroelasticity-based anemometer presented in this document [*Vonnegut, 1987, Waugh, 1966*].

---

[1] Product Specifications from:
NRG Systems Inc., NRG #40H Anemometer Specifications, 2008, <
http://www.nrgsystems.com/sitecore/content/Products/5930.aspx?pf=StandardSensors>
DAS Distribution, AR-816 Anemometer Specifications, n.d., < http://www.dasdistribution.com/products/anemometers/index.htm>
Calright Inc., General Tools WS821 Professional Wireless Weather Station, n.d., <http://www.calright.com/products/prod_id/1778/>
Extech Instruments Inc., Mini Thermo-Anemometer System Datasheet, 2008,
<http://www.testequipmentdepot.com/extech/pdf/45118_45158.pdf>

4.4 Implications for Aeroelastic Energy Harvesters

In addition to influencing the design of the anemometer prototype, the observations of section 2 also have some bearing on the design of aeroelastic energy harvesters such as those discussed in [*Allen et al. 2001*]. These include the 'fishtail' shape to increase instability (2.2), the influence of the upstream vortex street on the critical velocity and flutter amplitude (2.3), and the importance of flexural rigidity D in obtaining oscillation at low U_C. One observation not made by [*Dunnmon et al. 2011*] or [*Allen et al. 2001*] is that variable rigidity D would be critical to extracting maximum power from a variable wind source. Variable D would be advantageous both because of its importance to U_C and the importance of following the oscillator's analog to an engine's torque-speed efficiency maximum.

4.5 Theoretical Contributions to 'The Flag Problem'

In the course of investigating flutter phenomena to optimize the anemometer design, several observations were made which may have some bearing on the theoretical discussion of 'the flag problem'.

In section 2.3, it was found that the hysteresis U_C-U_D in the transition to flutter may be attributable to a discrete potential barrier between the flutter and non-flutter states. An upstream disturbance of arbitrarily large magnitude (such as a hand waved upstream of the filament) was sufficient to induce the filament to flutter at any velocity above the measured U_D. This is consistent with the view that the onset of the flutter instability requires a finite perturbation provided by the fluid. It was also noted that, as U was moved closer to U_C, the magnitude of the disturbance required to induce flutter decreased markedly. One interesting follow-up experiment may be to plot the magnitude of vortex energy density e supplied by a upstream disturbance at $U_D>U>U_C$ that is required to induce flutter. The slope of e (integrated over the flag area) vs. U may then be indicative of the particular 'activation energy' for the flag being tested. In addition to the activation energy description, section 2.3 also presented data suggesting that the conclusions of [*Wang, 2010*] –that a filament immersed in a vortex street will oscillated at the vortex frequency—may be incomplete, and that filaments do not oscillate at the Von-Karman frequency in all cases.

Section 2.7 also described how frequency dips observed at $U^* \sim=3\ U_C^*$ may correspond to the eigenvalue representing a 'second onset velocity' for most rectangular flags. Clearly, further experiments would have to be performed to validate this observation.

5. Conclusion

The flutter frequency of a thin plastic strip suspended parallel to fluid flow can provide a good indication of fluid velocity. A main advantage of this approach is scalability; because the onset of flutter is theoretically independent of the filament's characteristic length, a flowmeter based on this principle could possibly be manufactured down the micro scale. This effort focused on a mm-scale implementation of the aeroelastic oscillation-based anemometer. It was found that a 'fishtail' shaped filament with the maximum practical aspect ratio of ~10 was optimal. Additionally, the macro-scale prototype benefitted from a bluff body upstream of the filament; the optimal strength of the vortex-forcing occurred when the diameter of the bluff body was about half the length of the flag. Ultimately, the flutter frequency of a ~4mm filament mounted in a ~2cm flow-accelerating tube measured air flow to ±0.5m/s from 1-18 m/s and ±2m/s to 25m/s. Because the entire prototype system can be manufactured for less than $5, a next-generation oscillation-based anemometer system could be a successful product for a variety of flow measurement applications.

In addition the engineering work, several observations made in the course of this research could be of interest to the 'flag problem' in general. In particular, it was noted that the observed hysteresis in the transition to and from the flutter state may be explainable in terms of an activation energy that is usually provided by finite turbulence in the upstream flow.

6. Appendices

6.1 A Proof-of-Concept Prototype

In addition to the working prototype, an earlier prototype was inspired by the shape of a river fish, as shown in figure 32. This prototype was primarily a test of the systems integration prospects for an aeroelastic anemometer, and included a streamlined package, integrated compass, and limited user interface. While it is far larger than any realistic oscillation-based anemometer system, the lessons learned from its design and testing are applicable to the working prototype described in section 3.3.

Figure 32: *The integrated proof of concept measures 6 by 1.8cm.*

Mechanical Plant

There were two primary considerations in the design of the mechanical system.

1) Linearity: the system should be able to use the same element (the flapping fishtail) to measure both wind speed and direction. The entire system should also orient itself so as to measure wind in any direction.

2) Fluid Flow: Flow over the flag should be optimized per the analysis presented in section 3.1. The 'fish' body design should have sharp trailing edges to create a vortex street upstream of the flag.

In the proof-of-concept prototype, these goals were realized in the form of a fish-shaped electronics housing that connects directly to the streamer on the upstream side. A discrete phototransistor-laser diode combination takes the measurement and passes it to the main data processing unit through flexible servo wire routed through a bent aluminum stock. An intermediate housing contains a stationary compass chip and potentiometric position transducer, which combines the inclination of the revolving fish unit with the orientation of the aluminum stand to infer wind direction.

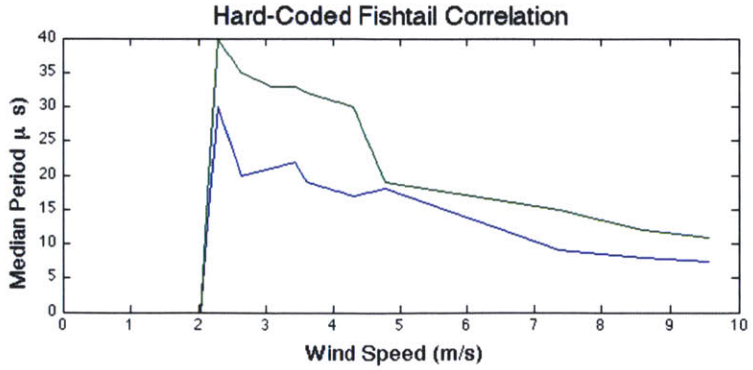

Figure 33: *The 'fishtail' was optimized per the analysis of section 2.2, with an additional biomimetic rear-end cutout. Its windspeed-median period correlation is shown. The blue trace is the absolute minimum, the green trace is the absolute maximum recorded; the hard-coded lookup table contains the mean of these two vectors.*

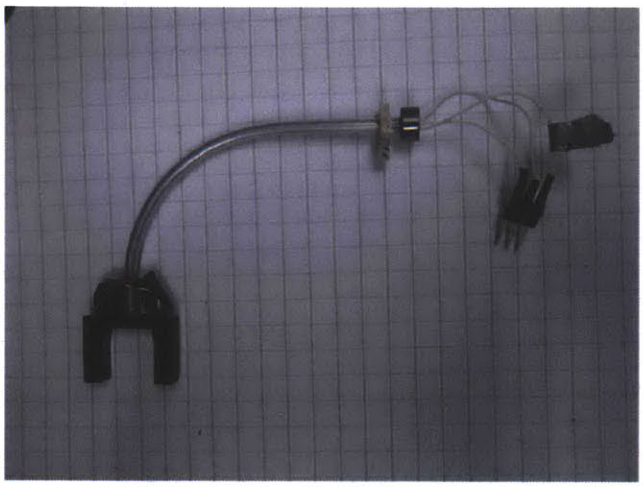

***Figure 34**: The naked stand with photointerrupt sensor, slip bearings and position transducer.*

Electrical Plant

The task of designing the electrical system was complicated by the goal of implementing the entire signal processing plant with simple, low-cost and low-power electronics that could eventually be integrated on a single small PCB. This made any 'development kit' or pre-built solution unattractive. There were five primary requirements for the electrical system:

1) A dynamic filter scheme. The system needed to be able to implement a robust filtering strategy for the potentially noisy data input from the streamer. Because the large fluttering streamer in this prototype tended to oscillate in a higher mode, the filtering was necessary to discern the fundamental frequency. In practice, a bubble-sort based median filtering routine worked for this purpose.

2) A large amount of RAM. With the fixed-window median sorting approach, the controller needs many RAM addresses to store a long vector of period lengths.

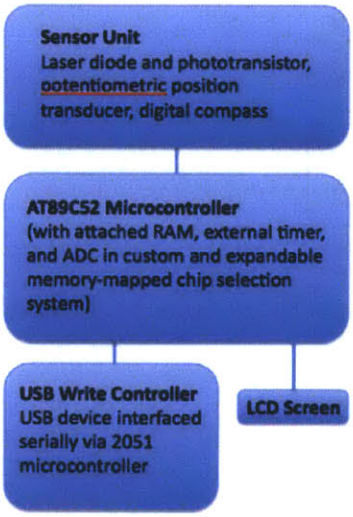

***Figure 35:** Block diagram of the proof-of-concept prototype electrical plant*

3) An analog-to-digital converter. Mounting a compass chip on the rotating streamer body was impractical for the amount of sliding contact points (12 lines to the digital compass) that it required. The digital compass was mounted at the base of the rotating anemometer dock, and use an analog position transducer (potentiometer with catch removed) to compare the compass output to the actual anemometer heading. The ADC was required to read the output of this position transducer.

4) A memory map. With the number of peripheral chips that could be introduced to streamline this system in the future (a frictionless digital position transducer, different types of sensors, more pins or a different data-collection system), it would have been very limiting not to introduce a way to easily add more peripheral chips.

5) Accessible long-term storage. This is useful to adjust the hard-coded wind-speed correlation with more precise computer analysis, and to more-closely mimic the form of an eventual anemometer product that would be useful to meteorologists collecting wind speed (or hydrologists collecting flow-rate) data.

Designing the electrical system required creating an embedded system from the 'ground up' based on an 8051 microcontroller. An overview is in figure 36, and the full plant is in figures 37 and 38.

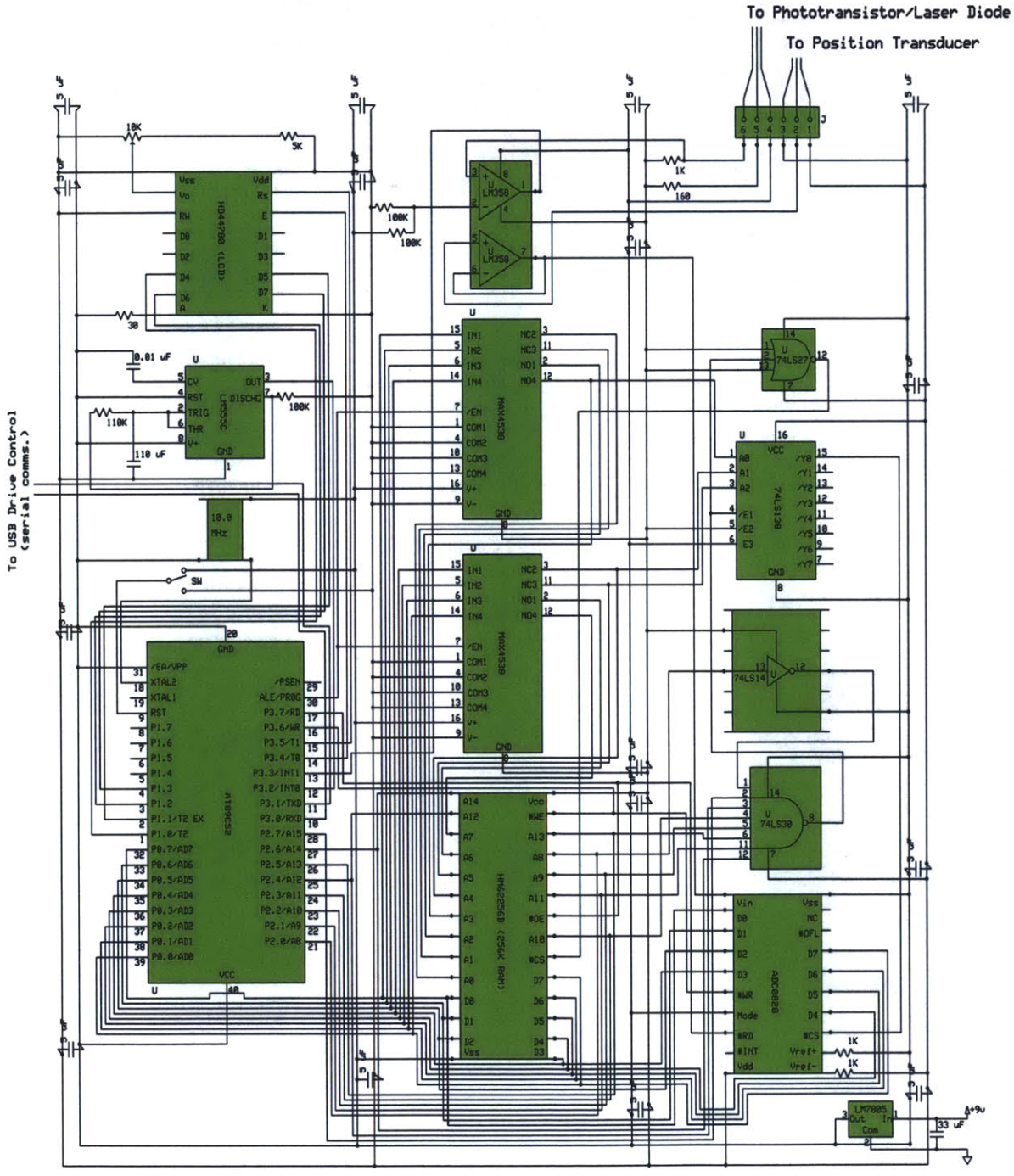

Figure 36: *The full electronics plant. While this unit was soldered on a 3x4" board, with modern integrated circuits a PCB implementation could easily fit inside the 'fish' itself.*

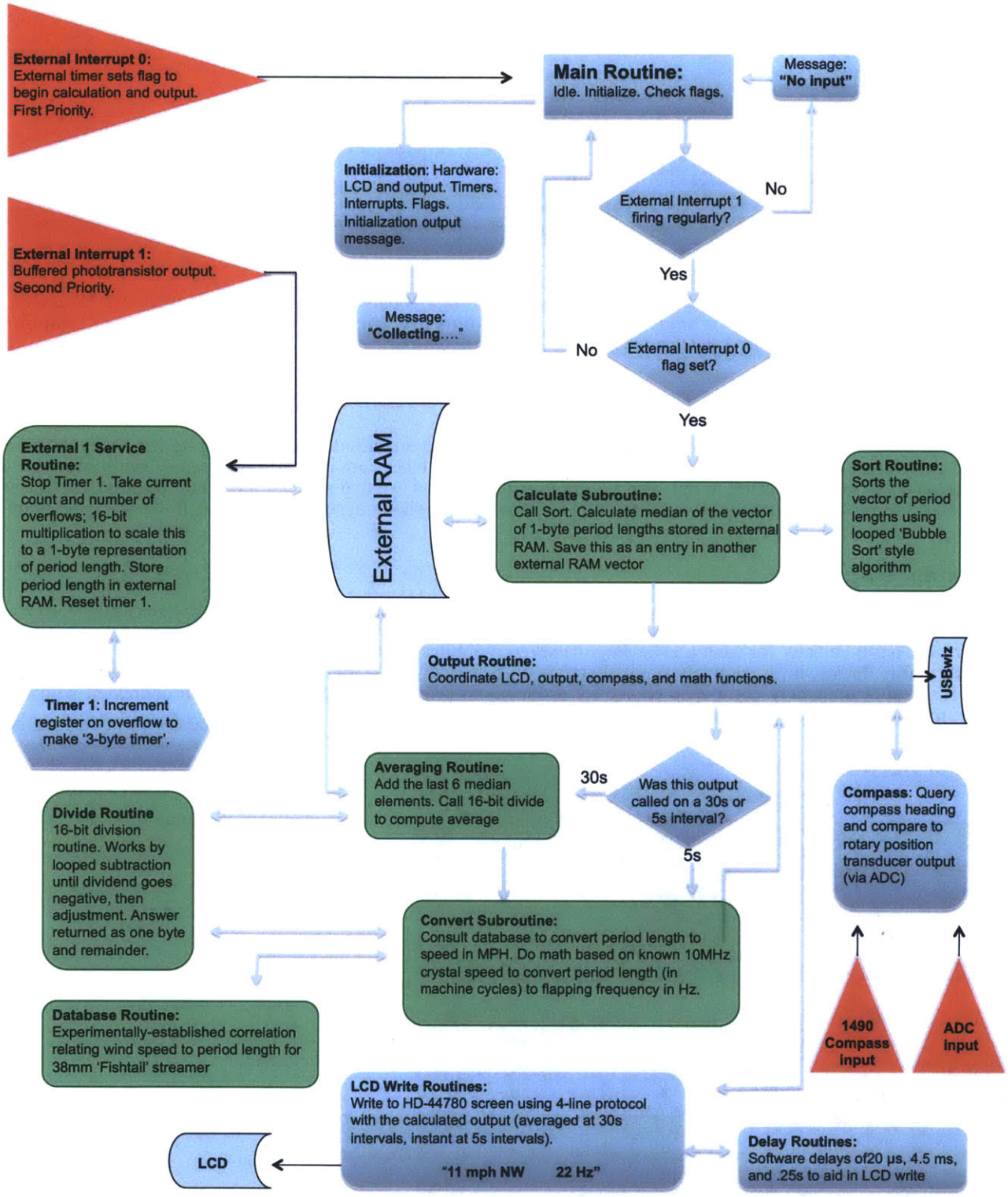

Figure 37: *Anemometer control code flowchart.*

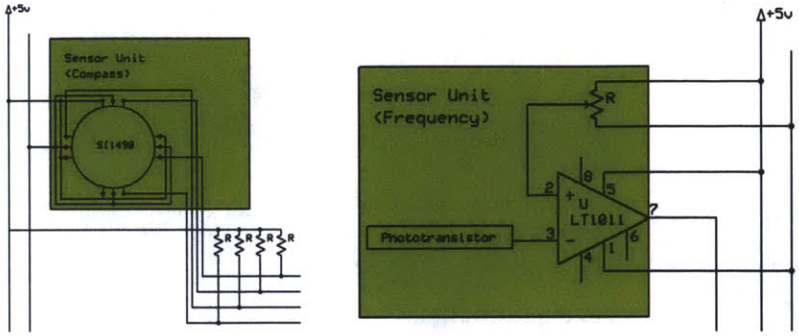

Figure 38: *Schematics of sensor units. The phototransistor/comparator is built into the 'fish' itself, while the Dinsmore 1490 digital compass is housed in the base station alongside the position transducer, with four pull-up resistors connecting its open collector outputs to four Port 1 pins on the AT89C52 (8051) controller.*

Software

The data processing code for the fishtail anemometer contained many math routines for managing the stream of incoming data. In the flowchart below, calculation-oriented routines and system blocks are indicated in green. 'Administrative' blocks are in blue, and external signals are in red. The system took data from 4 external sources: an analog position transducer (via ADC), an octal resolution digital compass, an external 555 timer, and a phototransistor. A software flowchart is in figure 38.

Performance Analysis

Based on 2 trials through the measurement range, the proof-of-concept anemometer system measures air flow to ±1.3m/s from 2 to 10 m/s. The system in operation is shown in video stills in figure 31. The system's primary drawbacks include i) a relatively high onset velocity for such a large flag, ii) severely limited upper range, because the filament exerts significant drag on the entire device, iii) a relatively fragile exterior. In particular, while the 'fish' shape is aesthetically attractive, the exposed filament is ultimately not a wise choice for a durable system. These drawbacks were all addressed with the first working prototype, described in section 3.3.

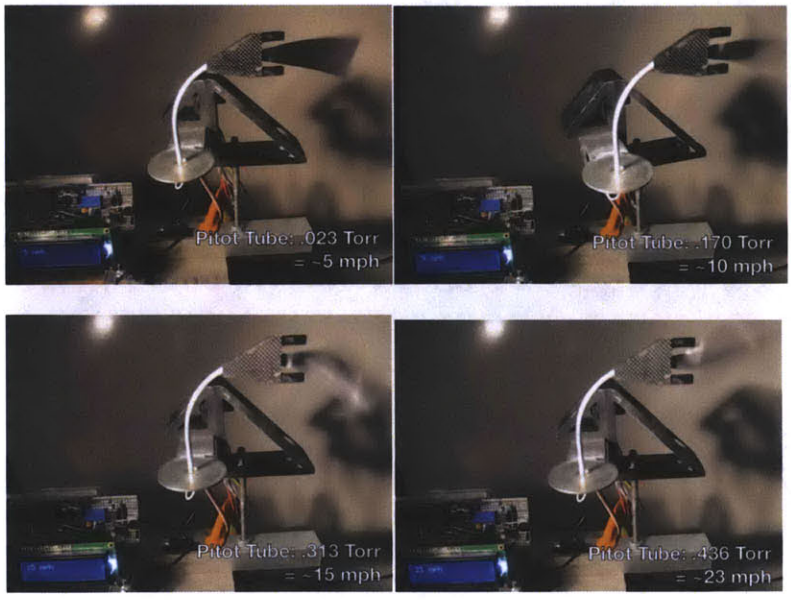

Figure 39: *Video stills of the proof-of-concept integrated prototype operating in a wind tunnel.*

References

S. Alben, *Flapping States of a Flag in an Inviscid Fluid: Bistability and the Transition to Chaos*, Physical Review Letters, vol. 100 (2008)

J. Allen, A. Smits, *Energy Harvesting Eel*. J. Fluids Struct. 15, 629–640 (2001)

M. Argentina and L. Mahadevan, *Fluid Flow-Induced Flutter of a Flag*, Proceedings of the National Academy of Sciences, vol. 102, no. 6 (2005)

C. Bao, C. Tang, X. Yin, *Flutter of Finite-Span Flexible Plates in Uniform Flow*, Chinese Physics Letters, vol.27, no.6 (2010)

D. Beal, F. Hover, M. Triantafyllou, J. Liao, G. Lauder, *Passive Propulsion in Vortex Wakes*. J. Fluid Mech. 549, 385–402 (2006)

D. Beal, G. Lauder, M. Triantafyllou, *Fish Exploiting Vortices Decrease Muscle Activity*. Science 302, 1566–1569 (2003)

I. Diaconu, D. Dorohoia, *Properties of Polyurethane Thin Films*, Journal of Optoelectronics and Advanced Materials Vol. 7, No. 2, p. 921 – 924 (2005)

J. Dunnmon, S. Stanton, B. Mann, E. Dowell, *Power extraction from Aeroelastic Limit Cycle Oscillations* Journal of Fluids and Structures 2011 **27 1182–1198 (2011)**

Dupont Corporation, *Mylar Datasheet*, 2006, <http://www.dupontteijinfilms.com/filmenterprise/Datasheet.asp?ID=302&Version=US>

Dupont Corporation, *Kapton Datasheet*, 1999, http://www.pleo.com/dupont/kap_thick.htm

J. Eldredge, D. Pisani, *Passive Locomotion of a Simple Articulated Fish-like System inthe Wake of an Obstacle* J. Fluid Mech. 607, 279–288, (2008)

C. Eloy, R. Lagrange, C. Souilliez, L. Schouveiler, *Aeroelastic Instability of CantileveredFlexible Plates in Uniform Flow* J. Fluid Mech. 611, 97–106 (2008)

Y. Fung, *An Introduction to the Theory of Aeroelasticity*, Dover Phoenix Editions, Mineola, NY (1969)

S. Gerrard, *The Wakes of Cylindrical Bluff Bodies at Low Reynolds Number*, Philosophical Transaction of the Royal Society of London, vol. 288 (1978)

S. Gerrard, *The Mechanics of the Formation Region of Vortices Behind Bluff Bodies*, J. Fluid Mech., 25:401-413, (1966)

L. Huang, *Flutter of Cantilevered Plates in Axial Flow* J. Fluids Struct. 9, 127–147 (1995)

A. Kornecki, E. Dowell, J. O'Brien, *On the Aeroelastic Instability of Two-Dimensional Panels in Uniform Incompressible Flow*. J. Sound Vib. 47 (2), 163-178 1976

Y. Kurimoto, M. Takeda, A. Koizumi, S. Yamauchi, S. Doi, Y. Tamura, *Mechanical Properties of Polyurethane Films Prepared from Liquefied Wood with Polymeric MDI*, Bioresource Technology, Volume 74, Issue 2, Pages 151-157, (2000)

C. Lemaitre, P. Hemon, E. de Langre, *Instability of a Long Ribbon Hanging in Axial Air Flow*, Journal of Fluids and Structures, vol. 20, (2005)

A. Manela, M. Howe *The Forced Motion of a Flag*, Journal of Fluid Mechanics, vol. 635 (2009)

J. Michelin, S.W. Smith, B. Glover, *Vortex shedding model of a flapping flag*, Journal of Fluid Mechanics, vol. 617 (2008)

R.W. Miller, *Flow Measurement Engineering Handbook*, McGraw Hill (1996)

Z. Pang, L. Jia, X. Jin, *Flutter Instability of Rectangle and Trapezoid flags in Uniform Flow*, Physics of Fluids, vol. 22, (2010)

M. Pa¨idoussis, *Fluid-Structure Interaction: Slender and Axial Flow*, Academic, London, (1998)

Lord Rayleigh, Proc. Lond. Math. Soc. X, 4–13. 3. (1879)

L. Shen, X. Zhang, D. Yue, M. Triantafyllou, *Turbulent Flow Over a Flexible Wall Undergoing a Streamwise Travelling Wave Motion*. J. Fluid Mech. 484, 197–221 (2003)

X. Su and F. Abdi, *Wrinkling Analysis of A Kapton Square Membrane under Tensile Loading*, 44th AIAA/ASME/ASCE/AHS Structures, Structural Dynamics, and Materials Conference (2003)

G. Taylor, J. Burns, S. Kammann, W. Powers, T. Welsh, *The Energy Harvesting Eel: a Small Subsurface Ocean/river Power Generator*. IEEE J. Ocean. Eng. 26, 539–547 (2001)

T. Theodorsen, *General Theory of Aerodynamic Instability and the Mechanism of Flutter*. Tech.Rep. No. 496, NACA. (1935)

B. Vonnegut, *Oscillatory Anemometer*, U.S. Patent 4671108 (1987)

S. Wang, J. Lai Bing, Y. Xie Zhen, *Kinematics and Forces of a Flexible Body in Karman Vortex Street,* Chinese Science Bulletin, vol. 54, no. 4 (2009)

Y. Watanabe, K. Isogai, S. Suzuki, M. Sugihara, *A Theoretical Study of Paper Flutter*, J. Fluids Struct. 16, 543–560 (2002)

C. Waugh, *Oscillating Vane Flowmeter,* U.S. Patent 3273389 (1966)

F. White, *Fluid Mechanics 6th ed.*, McGraw Hill (2008)

J. Zhang, S. Childress, A. Libchaber, M. Shelley, *Flexible Filaments in a Flowing Soap Film as a Model for One-Dimensional Flags in a Two-Dimensional Wind*, Nature, vol. 408 (2000)

L. Zhu and C. Peskin, *Simulation of a flapping flexible filament in a flowing soap film by the immersed boundary method.* Computational Physics (2002)